Geophysical Journal International

Geophys. J. Int. (2022) **230,** 870–892
Advance Access publication 2022 March 4
GJI Heat Flow and Volcanology

https://doi.org/10.1093/gji/ggac093

Stress changes caused by exsolution of magmatic fluids within an axisymmetric inclusion

Maria Elina Belardinelli, Massimo Nespoli and Maurizio Bonafede

Department of Physics and Astronomy, Alma Mater Studiorum, University of Bologna, 40126 *Bologna BO, Italy. E-mail: mariaelina.belardinelli@unibo.it*

Accepted 2022 March 2. Received 2022 February 24; in original form 2021 October 27

SUMMARY

In volcanic regions ascending magma is subject to depressurization and is generally accompanied by exsolution of volatiles. We assume a process in which these volatiles propagate upward across newly fractured and permeable rock layers, bringing a sharp increase of pore pressure and temperature within a thin disc-shaped region (inclusion). Thermo-poro-elastic (TPE) inclusion models provide a mechanism to explain seismicity and deformation induced by p and T changes in absence of new magma emplacement in volcanic contexts. They are also suitable to represent the mechanical effects due to fluid extraction and re-injection in geothermal fields. In the present work analytic solutions are provided for the displacement, strain and stress fields assuming a TPE unbounded medium. Significant deviatoric stress is generated by positive increments of pore pressure and temperature: the stress field is fully deviatoric outside the TPE inclusion, but a strong isotropic stress component is present within, leading to highly heterogeneous faulting mechanisms: if the disc plane is horizontal, thrust faulting mechanisms are favoured within the TPE disc over optimally oriented faults and normal mechanisms above. The model is easily generalized to a vertically thick disc with variable temperature and pore-pressure changes: then, an extensional environment can be obtained even within the TPE inclusion assuming upward decreasing of pore pressure and temperature changes. The supplied analytical solution may be used to model near-field TPE inclusion effects and to validate more complex numerical modelling.

Key words: Permeability and porosity; Hydrothermal systems; Induced seismicity; Mechanics, theory, and modelling; Volcanic gases.

1 INTRODUCTION

It is well known in Earth sciences that temperature changes accompanying erosion and sedimentation processes have a strong influence on the stress field and fault mechanisms within the upper crustal layers (e.g. Turcotte & Schubert 2014). Nevertheless, the role of temperature changes, T, in triggering and characterizing seismic activity (e.g. Schlindwein *et al.* 2013) within geothermal and volcanic regions is often undervalued. Important and widespread effects are also provided by pore pressure changes, p, within permeable rock layers (e.g. Shapiro 2015). At equilibrium, the inclusion method described by Eshelby (1957) allows us to model the mechanical effects of pore-pressure and temperature changes occurring inside a closed volume (i.e. an inclusion) embedded in an elastic medium. Such an approach can be used, for example, for modelling the deformation and the stress field induced by geothermal reservoirs (Geertsma 1973; Segall 1992; Rudnicki 1999; Guido *et al.* 2015).

The Eshelby's approach is well known also because it provides an explanation for the heterogeneity of fault mechanisms induced by oil and gas production, where normal and thrust events occur at close distance from each other, inside and around the reservoir (Segall 1989; Segall & Fitzgerald 1998). Although most of the literature focuses on applications to induced seismicity due to reservoir exploitation, heterogeneities of fault mechanisms are observed even in volcanological contexts, as for example the Campi Flegrei caldera in Italy (D'Auria *et al.* 2014; Nespoli *et al.* 2021) or the Tatun Volcano Group in Northern Taiwan (Pu *et al.* 2021). An extreme variability of fault mechanisms is observed in several tectonically and geothermally active regions of the world such as the South Iceland Seismic zone (e.g. Lund *et al.* 2005; Stefansson *et al.* 2011) and the geothermal field of the Krafla volcano, in North East Iceland (Schuler *et al.* 2016). Often, the explanation of the heterogeneity of focal mechanisms in volcanological environments is ascribed to the stress changes induced by magmatic sources of deformation (e.g. D'Auria *et al.* 2014). In the present work we interpret the heterogeneity of fault mechanism as due to purely thermo-poro-elastic (TPE) effects generated by an inclusion where changes p and T in pore pressure and temperature, respectively, occur.

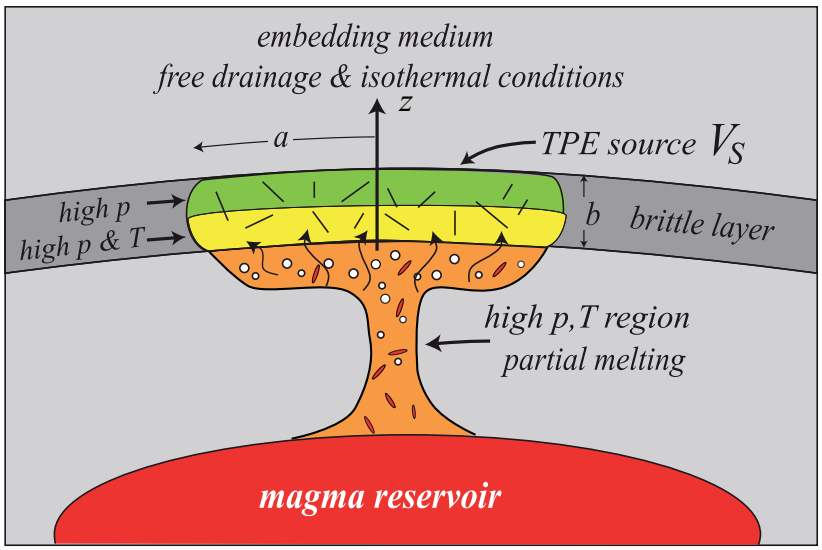

Figure 1. Conceptual model of a TPE source region (yellow–green), with a small thickness b and radius a, undergoing a sudden increase of permeability due to seismic fractures. The upward migration of previously trapped fluids of magmatic origin (white bubbles) from the underlying partially molten material (orange) is accompanied by high p, T changes within the TPE source, triggering further seismicity according to a positive feedback mechanism.

While in reservoir exploitation p and T are anthropically induced (injection and production from wells), in a volcanological context they can derive from the exsolution of magmatic fluids, as suggested by the recent literature (Nespoli *et al.* 2021) about the caldera of Campi Flegrei (Italy). Recently, Todesco (2021) has shown that the deformation history during the last 35 years, following the major uplift during 1982–1984, can be ascribed to a poro-elastic behaviour of the shallow hydrothermal system of Campi Flegrei, suggesting that fluids have an important role in the ongoing unrest. Most of the literature agrees in assigning an important role to the mechanical effects induced by magmatic fluids both in the deformation and stress field that characterize the caldera of the Campi Flegrei. For the 1982–1984 unrest, the position and geometry of a TPE inclusion was inferred by Nespoli *et al.* (2021) by inversion of geodetic data. They also found that most of relocated hypocentres during this period are within the TPE inclusion, which will be shown to be the region of maximum induced shear stress. A direct involvement of fluids was also assumed for the seismic swarm occurred at Campi Flegrei in July 2000 (Saccorotti *et al.* 2001), which was associated with the upward migration of a pressure front, triggered by an excess of fluid pressure from a magmatic intrusion (Bianco *et al.* 2004).

In the following, we assume a scenario in which volatiles of magmatic origin rise towards the surface by crossing a brittle layer (Fig. 1). In volcanic regions ascending magma is subject to depressurization and is generally accompanied by exsolution of volatiles (mostly H_2O and CO_2) at high temperature and pressure which can efficiently migrate across fissures and cracks of the embedding rock, providing significant flows of fluid mass and heat. Due to the lower density and viscosity of volatiles, the pressure decrease accompanying their upward migration is smaller than the 'magmastatic' decrease of pressure of ascending basaltic magma. Accordingly, the migration of volatiles is expected to be faster and more efficient than magma uprise. An increasing deviatoric stress, possibly due to tectonic deformation (e.g. Belardinelli *et al.* 2011) and/or to new magma emplacement (e.g. Trasatti *et al.* 2011), is assumed to generate seismic fractures within the brittle layer which provide a substantial increase of permeability. The permeability change plausibly takes place progressively during seismic activity but, for the sake of mathematical simplicity, we shall assume that it takes place suddenly, following the breaching of an impervious barrier initially present at the base of the brittle layer. Then, upward migration of magmatic fluids is allowed, bringing a sharp increase of pore pressure, temperature and seismicity. Such a scenario can be assumed for example for the Campi Flegrei caldera (Lima *et al.* 2021) and is consistent with the enhanced seismic tomography studies of Calò & Tramelli (2018). A similar scenario was proposed by Zencher *et al.* (2006) to explain earthquake triggering by fluids uprising from the brittle–ductile transition in the South Iceland Seismic Zone. Unlike the model of Zencher *et al.* (2006), we consider that the region affected by increases of p and T is finite volume (Fig. 1) as in Belardinelli *et al.* (2019). Even if both changes in pore pressure and temperature provide formally similar incremental stresses, because they are obtained from similar constitutive relationships, they obey different propagation equations (e.g. Bonafede & Mazzanti 1997; Nespoli *et al.* 2021). Furthermore only pore pressure changes affect explicitly the Coulomb failure function change, and then the induced seismicity, as already shown in Belardinelli *et al.* (2019).

A realistic description of the proposed scenario requires accounting for the complex properties of the solid and fluid phases and their mutual interactions, but its quantitative implementation represents a formidable task even when resorting to numerical methods. In fact, as we shall see in the following, even a linear theory for a homogeneous TPE medium requires at least 12 material constants to characterize the thermomechanical properties of the rock and fluid. Moreover temperature changes may be enhanced by latent heat release if phase transitions take place within propagating fluids and this may considerably extend the spatial domain of temperature changes. The increasing pore pressure, in turn, is expected to open fissures and cracks wider as suggested by Zencher *et al.* (2006) and to trigger induced seismicity,

thus providing a positive feedback mechanism between pore pressure, seismicity and effective permeability. However both the geometrical distribution of permeability and its evolution following seismic events are generally unknown and difficult to model (e.g. Gischig *et al.* 2014; Rinaldi & Nespoli 2017). As in any class of problems, an effective strategy consists in starting from simple cases and then moving towards increasing complexity. The purpose of the present paper is to provide fully analytical solutions to model the TPE effects of the volume where exsolved hot and pressurized magmatic volatiles accumulate, by representing it as a TPE inclusion embedded in an unbounded homogeneous medium. The proposed solution can be used to model the mechanical state attained by the medium at a given instant of time during the exsolution of magmatic fluids inside the TPE inclusion. At this time p and T are the changes of pore pressure and temperature with respect to the configuration before the beginning of exsolution. While in Belardinelli *et al.* (2019) the TPE inclusion has a spherical symmetry, in this paper it is assumed disc-shaped, which is considered a more realistic geometry. Moreover we shall account for different spatial extensions of temperature and pore-pressure changes (Fig. 1) within the TPE inclusion. We also show how p and T are expected to evolve with time under the simplified assumption of a 1-D vertical propagation with constant permeability without phase transitions.

The advantage in assuming an unbounded medium is that exact analytic solutions may be derived in this framework for the deformation and stress fields; the obtained solution has several similarities with the uniform opening dislocation problem (mode I) but has also important differences. Another important result, valid in an unbounded medium, is that a simplified diffusion equation may be obtained for the pore pressure, formally independent from stress, as already noted by Shapiro (2015) and Wang (2017). Neglecting the presence of the free surface may appear unrealistic but Mantiloni *et al.* (2020) provided semi-analytical solutions for a disc-shaped TPE source in a homogeneous half-space as the sum of different terms, showing that the term which describes the effect of a TPE disc embedded within an unbounded medium is dominant close to and within the disc.

Analytical solutions of simple boundary-value problems allow exploring quickly the effects of various properties and their mutual interactions. Furthermore, the analytical solutions allow us to distinguish phenomena due to the boundary conditions from the consequences of the material response, while the theory generally provides an environment inside which additional complications may be implemented, if necessary. Finally, complex geometries, medium heterogeneities (e.g. Minakov & Yarushina 2021) and the inclusion of non-linear effects inevitably require the use of numerical analysis techniques (e.g. Nespoli *et al.* 2021) and the exact solutions of simple particular cases are invaluable for the validation of computer codes. An additional strength of an elastic analytical solution, is that a generalization to a viscoelastic behaviour may be obtained using the correspondence principle (Fung 1965).

2 CONSTITUTIVE TPE RELATIONSHIPS

The strain field ϵ_{ij} in a TPE medium which undergoes a change of stress τ_{ij}, a change of pore pressure p and a change of temperature T, with respect to an initial configuration of equilibrium, is provided by the following constitutive relation (e.g. Biot 1941; McTigue 1986):

$$\epsilon_{ij} = \frac{1}{2\mu}\left(\tau_{ij} - \frac{\nu}{1+\nu}\tau_{kk}\delta_{ij}\right) + \frac{1}{3H}p\delta_{ij} + \frac{1}{3}\alpha_s T\delta_{ij}, \tag{1}$$

where μ is the rigidity of the medium, ν the drained isothermal Poisson ratio, $1/H$ is the poroelastic expansion coefficient, as defined by Biot (1941) and α_s is the coefficient of thermal expansion in drained conditions (equal to the thermal expansion of the solid skeleton). In eq. (1) and hereinafter we use the Einstein's notation which implies the summation on repeated indices.

The 'stress-free strain' (i.e. the strain produced by T and p in absence of stress) is simply:

$$\epsilon_0\,\delta_{ij} = \left(\frac{1}{3H}p + \frac{1}{3}\alpha_s T\right)\delta_{ij}. \tag{2}$$

We observe that ϵ_0 depends linearly on T and p changes inside the inclusion and will be referred as 'TPE inclusion potency' since displacement, strain and stress will be shown to be proportional to ϵ_0. The inverse relation providing τ_{ij} in terms of ϵ_{ij}, p and T is simply obtained from eq. (1) and eq. (2) as

$$\tau_{ij} = 2\mu\left\{\epsilon_{ij} + \frac{1}{1-2\nu}\left[\nu\epsilon_{kk} - (1+\nu)\epsilon_0\right]\delta_{ij}\right\}. \tag{3}$$

As shown by Rice & Cleary (1976) the constant H may be computed from the bulk modulus $K = \frac{2\mu(1+\nu)}{3(1-2\nu)}$ of the porous medium in drained isothermal conditions and the unjacketed bulk modulus K_s', according to the relation

$$\frac{1}{H} = \frac{1}{K} - \frac{1}{K_s'}, \tag{4}$$

K_s' can be interpreted as the bulk modulus of the solid phase with good approximation (Rice & Cleary 1976; Wang 2017).

Following Rice & Cleary (1976), a different description of the poro-elastic properties may be used, in which the Skempton parameter B (Skempton 1954) and the undrained Poisson ratio ν_u appear. The Skempton parameter B describes the pore pressure induced by a change of isotropic stress in undrained and isothermal conditions

$$\Delta p = -\frac{B}{3}\tau_{kk} \qquad \text{(undrained and isothermal conditions)} \tag{5}$$

which allows writing the undrained Poisson ratio in isothermal conditions, from eq. (1), as

$$\nu_u = \frac{3\nu + B(1-2\nu)\frac{K}{H}}{3 - B(1-2\nu)\frac{K}{H}}. \tag{6}$$

3 METHOD OF SOLUTION FOR THE DISPLACEMENT FIELD

As shown in detail by Belardinelli *et al.* (2019), the equilibrium displacement field u_i produced by a localized uniform increase of temperature T and pore-pressure p within a TPE source volume V_S may be computed according to the inclusion method described by Eshelby (1957) as

$$u_i(\mathbf{x}) = 3K\epsilon_0 \int_{V_s} \frac{\partial G_{ik}(\mathbf{x}, \mathbf{x}')}{\partial x_k'} \mathrm{d}V', \tag{7}$$

where $G_{ik}(\mathbf{x}, \mathbf{x}')$ is the drained isothermal Green's function in an elastic medium. Clearly $G_{ik}(\mathbf{x}, \mathbf{x}')$ is given by the same expression which applies in a purely elastic medium if an isothermal process in free drainage conditions is considered, provided that ν is the drained isothermal Poisson ratio. It is worth noting that, according to eq. (1), the deviatoric strain does not depend on p and T (Fjær *et al.* 2008; Shapiro 2015). If we assume that the embedding medium is elastic, unbounded and homogeneous, we have (e.g. Landau & Lifshits 1967)

$$G_{ik}(\mathbf{x}, \mathbf{x}') = \frac{1}{16\pi\mu(1-\nu)} \left[(3-4\nu)\frac{\delta_{ik}}{r} + \frac{(x_i - x_i')(x_k - x_k')}{r^3} \right], \tag{8}$$

where $r = |\mathbf{x} - \mathbf{x}'|$ is the distance between $\mathbf{x}$ and $\mathbf{x}'$. Exploiting the property $G_{ik}(\mathbf{x}, \mathbf{x}') = G_{ik}(\mathbf{x} - \mathbf{x}')$ (valid for a homogeneous unbounded medium) we obtain by straightforward calculation

$$\frac{\partial G_{ik}(\mathbf{x}, \mathbf{x}')}{\partial x_k'} = -\frac{\partial G_{ik}(\mathbf{x}, \mathbf{x}')}{\partial x_k} = -\frac{1-2\nu}{8\pi\mu(1-\nu)} \frac{\partial}{\partial x_i}\left(\frac{1}{r}\right) \tag{9}$$

and eq. (7) may be rewritten in vector form as

$$\mathbf{u}(\mathbf{x}) = -\epsilon_0 \frac{(1+\nu)}{4\pi(1-\nu)} \nabla \left[\int_{V_s} \frac{1}{|\mathbf{x} - \mathbf{x}'|} \mathrm{d}V' \right] = -\frac{\epsilon_1}{4\pi} \nabla\Phi, \tag{10}$$

where the relation $K = \frac{2\mu(1+\nu)}{3(1-2\nu)}$ for the drained isothermal bulk modulus was used and

$$\Phi(\mathbf{x}) = \int_{V_s} \frac{1}{|\mathbf{x} - \mathbf{x}'|} \mathrm{d}V', \qquad \epsilon_1 = \epsilon_0 \frac{(1+\nu)}{(1-\nu)}. \tag{11}$$

From eqs (10), (11) and $\nabla^2 r^{-1} = -4\pi\delta(\mathbf{x} - \mathbf{x}')$ we see that

$$\nabla \cdot \mathbf{u} = -\frac{\epsilon_1}{4\pi}\nabla^2\Phi = \epsilon_1 \int_{V_s} \delta(\mathbf{x} - \mathbf{x}')\mathrm{d}V' = \begin{cases} \epsilon_1 \text{ if } \mathbf{x} \in V_s \\ 0 \text{ otherwise,} \end{cases} \tag{12}$$

where $\delta(\mathbf{x} - \mathbf{x}')$ is Dirac's delta, so that ϵ_1 is the dilatation in the interior of the TPE source while the strain field is purely deviatoric outside. Accordingly, the displacement potential Φ obeys the Poisson equation $\nabla^2\Phi_S = -4\pi$ within the TPE source region V_S (where $\Phi \equiv \Phi_S$) and the Laplace equation $\nabla^2\Phi_{el} = 0$ in the elastic region V_{el} surrounding V_S (where $\Phi \equiv \Phi_{el}$), which is assumed in isothermal and free drainage conditions.

The medium which embodies the TPE inclusion volume V_S can be assumed drained or elastic in two different scenarios:

(i) The external medium is assumed to be in hydrostatic isothermal conditions. This is reasonable if, as in Nespoli *et al.* (2021), the fluid flow is large enough to dissipate efficiently incoming heat and pore pressure. This can occur if the inclusion is placed just below a high permeability aquifer as suggested by observations at Campi Flegrei (Calò & Tramelli 2018) and assumed in the model of Nespoli *et al.* (2021). In this case, the internal region adjusts the boundary condition of near-lithostatic pore pressure present below its bottom to the near hydrostatic value present within the aquifer above (e.g. Lima *et al.* 2021).
(ii) The external medium is assumed to be elastic and with low permeability. This happens when no variations of pore pressure and temperature occur in the external region, as expected in geothermal environments (e.g. Guido *et al.* 2015; Wangen & Halvorsen 2020), where the reservoir, that is the inclusion, is hydraulically confined. Accordingly, the timescale for fluids to diffuse outside V_S is much longer than the one needed to diffuse within V_S.

Displacements and tractions must be continuous across the surface Σ enclosing V_S; thus Φ must be continuous with continuous derivatives across Σ. In particular $\nabla\Phi_S = \nabla\Phi_{el}$ on Σ.

It may be added that the continuity of tractions $\tau_{ij}n_j$ across Σ is already fulfilled according to Eshelby's inclusion procedure and requires, according to eqs (3) and (12), a discontinuity in the second derivatives of the potential, since $\epsilon_{ij} = -\frac{\epsilon_1}{4\pi}\frac{\partial^2\Phi}{\partial x_i \partial x_j}$:

$$\left[\frac{\partial^2\Phi_{el}}{\partial x_i \partial x_j} - \frac{\partial^2\Phi_S}{\partial x_i \partial x_j} \right]_\Sigma n_j = 4\pi n_i. \tag{13}$$

This requires that the linear dilatation/contraction $\epsilon_{nn} = \epsilon_{ij} n_i n_j$ in the normal direction of Σ is discontinuous across the boundary. The jump amplitude is $-\epsilon_1$, so that contraction is predicted outside and dilatation inside Σ, along the normal direction n_i.

We note that eq. (7) provides the equilibrium displacement for a given ϵ_0, or given temperature and pore pressure changes. Following energy balance and transport equations it is possible to model how the TPE inclusion potency ϵ_0, that is p and T, evolves with time, as shown in the next section.

4 HINTS AND FIELD EQUATIONS FOR MODELLING THE EVOLUTION OF p AND T

For the sake of simplicity we assume an initial configuration within the brittle layer in which the pore-pressure has a hydrostatic gradient and the temperature is uniform. In this case the total temperature $T^{\mathrm{TOT}}(\mathbf{x}, t)$, equals the temperature variation T, apart from an inessential constant value. Such an assumption is justified if the temperature increase at the base of the TPE layer appears within a time much shorter than the characteristic conductive timescale. The space–time evolution of pore-pressure and temperature changes, p and T, are described by the following equations (e.g. Bejan 1984). The first equation is the fluid mass continuity equation:

$$\frac{\partial \rho_f}{\partial t} + \nabla \cdot (\rho_f \mathbf{q}) = 0, \tag{14}$$

where t is time, ρ_f is fluid density and $\mathbf{q}$ is the specific discharge rate, that is the volume of fluid crossing the unit surface in a unit of time. The second equation is the phenomenological Darcy law, an empirical relation between the pressure gradient and the specific discharge rate

$$\mathbf{q} = -\frac{k}{\eta} \nabla p, \tag{15}$$

where k is the permeability of the solid matrix, η is fluid viscosity and p is assumed as the fluid pressure in excess of the hydrostatic value p_h (with $\nabla p_h = \rho_f \mathbf{g}$). The third equation is the mechanical equilibrium equation which, considering the stress change τ_{ij} superposed onto the configuration of gravitational equilibrium (e.g. a lithostatic configuration), reads

$$\frac{\partial \tau_{ij}}{\partial x_j} = 0. \tag{16}$$

The fourth equation is the energy balance for the whole system (e.g. Bejan 1984), in which local thermal equilibrium is assumed between the solid matrix (with porosity ϕ, density ρ_s specific heat c_s, thermal conductivity λ_s) and the fluid (with specific heat c_f, conductivity λ_f):

$$\rho c \frac{\partial T}{\partial t} + \rho_f c_f \mathbf{q} \cdot \nabla T = \lambda \nabla^2 T - \mathbf{q} \cdot \nabla p, \tag{17}$$

where $\rho c = [\phi \rho_f c_f + (1 - \phi)\rho_s c_s]$ and $\lambda = [\phi \lambda_f + (1 - \phi)\lambda_s]$ denote average specific heat per unit volume and average conductivity, respectively. In eq. (17) the heat transferred by conductive processes, $\lambda \nabla T^2$ and the mechanical work rate $\mathbf{q} \cdot \nabla p$ done on the unit fluid volume, which is converted into heat through viscous dissipation, are written in the right-hand side (r.h.s.).

The set of equations is completed by the fully contracted compatibility equation, $\nabla^2 \epsilon_{kk} - \frac{\partial^2}{\partial x_i \partial x_k} \epsilon_{ik} = 0$, which can be merged with the fluid mass conservation (eq. 14) to provide the following equation (e.g. McTigue 1986)

$$\left[\frac{\partial}{\partial t} - D\nabla^2\right]\left(\tau_{kk} + \frac{3}{B} p\right) = D\beta_1 \nabla^2 T + \beta_2 \frac{\partial T}{\partial t}, \tag{18}$$

where D is the hydraulic diffusivity

$$D = \frac{k\mu}{\eta} f(B, \nu, \nu_u), \qquad \text{with} \quad f(B, \nu, \nu_u) = \frac{2B^2(1 + \nu_u)^2(1 - \nu)}{9(1 - \nu_u)(\nu_u - \nu)}$$

and

$$\beta_1 = \mu \alpha_s \frac{4}{3} \frac{1 + \nu}{1 - \nu}, \quad \beta_2 = 2\mu B \phi (\alpha_f - \alpha_s) \frac{(1 + \nu)(1 + \nu_u)}{3(\nu_u - \nu)}.$$

In the previous equation α_s, α_f are thermal expansion coefficients for the solid and fluid phase, respectively. The term multiplied by β_1 describes purely thermo-elastic effects and it is present in the compatibility equation of thermoelastic equilibrium in absence of fluids (e.g. when $\phi = 0$). The term multiplied by β_2 describes the effects of the fluid contained inside the pores. The factor $f(B, \nu, \nu_u)$ has order of magnitude 1 so that $D \sim \frac{k\mu}{\eta}$. Inserting $\epsilon_{kk} = \epsilon_1$ (from eq. 12) into the constitutive relationship, we find $\tau_{kk} = -4\mu\epsilon_1 = -4\mu\epsilon_0(1 + \nu)/(1 - \nu)$, so that τ_{kk} appearing in eq. (18) can be rewritten in terms of p and T. As a consequence of that, the term proportional to $\nabla^2 T$ appearing in the left-hand side of eq. (18) cancels with the term multiplied by β_1 in the r.h.s. Taking into account the relationship between poro-elastic parameters, $H = 2\mu B(1 + \nu_u)(1 + \nu)/(9\nu_u - 9\nu)$ (e.g. Wang 2017), the following diffusion equation is obtained for the pore pressure:

$$\left(\frac{\partial p}{\partial t} - D\nabla^2 p\right) = (\gamma_1 + \gamma_2) \frac{\partial T}{\partial t}, \tag{19}$$

where

$$\gamma_1 = \frac{4}{9} \mu B \alpha_s \frac{(1 + \nu_u)}{(1 - \nu_u)} \qquad \gamma_2 = \frac{2}{9} \mu B^2 \phi (\alpha_f - \alpha_s) \frac{(1 - \nu)(1 + \nu_u)^2}{(1 - \nu_u)(\nu_u - \nu)}.$$

Thus, the term proportional to γ_2 describes the pore pressure induced by a sudden increase of temperature in undrained conditions, due to the greater thermal expansion of the fluid with respect to the thermal expansion of pores. The term proportional to γ_1 is present even when $\alpha_f = \alpha_s$; it may be understood as arising, in undrained conditions, from the compression of the solid matrix, undergoing thermal dilatation constrained by the embedding medium.

4.1 The case of a flat TPE inclusion

In this paragraph, we assume a flat TPE inclusion with a thickness b, as the yellow-green region shown in Fig. 1, and the case of scenario 1 (Section 3). The complete set of equations described in the previous section is rather complex and non-linear terms $\mathbf{q} \cdot \nabla T$, $\mathbf{q} \cdot \nabla p$ appear in eq. (17). However the two terms in the r.h.s. of eq. (17) are negligible in high permeability ($k > 10^{-13}$ m^2, e.g. Wang 2017) media endowed with normal thermal conductivity ($\lambda \sim$ a few Wm^{-1}K^{-1}, e.g. Turcotte & Schubert 2014), undergoing temperature changes $\Delta T \sim 100$ K and pressure changes $\Delta p \sim 10^7$ Pa. Values of $\Delta T \sim 10^2$ K and $\Delta p \sim 10^7$ Pa seem plausible in proximity of magma reservoirs. There the temperature is up to 10^3 K (e.g. Sigurdsson *et al.* 1999) greater than typical mid-crustal values and the release of volatiles from magma reservoirs at a few km depth, subject to near-lithostatic pressure, may occur. Furthermore, the mechanical strength of basaltic rock is generally evaluated in the order of ∼10 MPa (e.g. Heap *et al.* 2021), then we expect that p can be up to this value, otherwise below the TPE region (Fig. 1), tensile failure (hydrofracture) of basaltic rocks would occur, drastically reducing p. For example, if we consider water substance ($\rho_f c_f \approx 4.2 \times 10^6$ Jm^{-3} K^{-1}), we see that the dissipative heat production $\mathbf{q} \cdot \nabla p \sim \frac{k}{\eta b^2} \Delta p^2$ in the r.h.s. of eq. (17) is more than 2 orders of magnitude smaller than the advective term $\rho_f c_f \mathbf{q} \cdot \nabla T \sim \frac{k}{\eta b^2} \rho_f c_f \Delta p \Delta T$. Moreover, thermal conduction $\lambda \nabla^2 T \sim \lambda \Delta T / b^2$ is ∼4 orders smaller than heat advection for $\eta = 10^{-3}$ Pa s; then, both terms can be neglected and the following initial and boundary value problem is obtained referring to Fig. 1.

$$\rho c \frac{\partial T}{\partial t} + \rho_f c_f \mathbf{q} \cdot \nabla T = 0 \qquad \begin{cases} \text{with B.C. } T(0, t) = \Delta T \\ \text{and I.C. } \quad T(\zeta, 0) = 0 \end{cases}, \tag{20}$$

where $\zeta = 0$ at the bottom of the TPE inclusion region. If after the beginning of exsolution ($t > 0$), $\mathbf{q}$ were nearly constant, the solution would be:

$$T = \Delta T \left[1 - \Theta(s - V_T t)\right], \tag{21}$$

where $\Theta(x)$ is the Heaviside step function ($\Theta(x) = 0$ if $x < 0$, $\Theta(x) = 1$, if $x > 0$), s denotes the abscissa along the fluid streamlines and $V_T = \frac{\rho_f c_f}{\rho c} q$ is the speed of the temperature front. If thermal conduction were considered in eq. (17), the equation might be solved using the technique of separation of variables, providing a solution as an infinite series: the temperature front would not be strictly discontinuous, but the transition from ΔT to zero would take place within a narrow spatial range $\sim \sqrt{\lambda t/(\rho c)}$ (a few meters even after several years). Neglecting heat conduction across the lateral impervious boundary of the TPE region, we may consider s vertical so that both T and p are functions of the vertical coordinate ζ and time t only. The temperature front reaches the top the TPE region at $\zeta = b$ in a time $t_T = b/V_T$.

Inserting eq. (21) into eq. (19) for pressure, we may consider the following boundary value problem for $p(\rho, \zeta, t)$:

$$\left(\frac{\partial}{\partial t} - D\nabla^2\right) p = (\gamma_1 + \gamma_2) V_T \Delta T \delta(\zeta - V_T t) \qquad \begin{cases} \text{with B.C. } p = \Delta p \quad \text{in } \zeta = 0, \forall t \geq 0 \\ \qquad\qquad p = 0 \quad \text{in } \zeta = b, \forall t \geq 0 \\ \qquad\qquad \frac{\partial p}{\partial \rho} = 0, \quad \text{in } \rho = a, \forall t \geq 0 \\ \text{and I.C. } \quad p = 0 \quad \text{in } 0 < \zeta < b, \rho < a, \forall t = 0 \end{cases} \tag{22}$$

where the lateral boundary $\rho = a$ is assumed impervious to fluid flow, so that $\partial p/\partial \rho = 0$. This problem is compatible with the previous assumption that p is a function of ζ and t only, confirming that the streamlines are along the vertical direction.

The problem (22) was solved using the technique of separation of variables (Fig. 2) but an accurate approximate solution may be found since t_T is several orders of magnitude longer than the characteristic pressure diffusion time $t_p = b^2/D$; indeed we have

$$t_T = \frac{b}{V_T} \sim \frac{b^2 \eta}{k \Delta p} \frac{\rho c}{\rho_f c_f}, \qquad t_p = \frac{b^2}{D} \sim \frac{b^2 \eta}{k \mu f(B, \nu, \nu_u)} \tag{23}$$

thus, $t_p/t_T \sim \Delta p/\mu \ll 1$. For example, for Berea sandstone, which is a highly porous rock, $\mu = 6$ GPa (Wang 2017; Rice & Cleary 1976) and we get $t_p/t_T = 8 \times 10^{-4}$). Then a quasi-static approximation is appropriate for $t > t_p$ (Fig. 2b), where eq. (22) becomes $\frac{\partial^2 p}{\partial \zeta^2} \simeq -\frac{\gamma_1 + \gamma_2}{D} V_T \Delta T \delta(\zeta - V_T t)$ with the following simple solution:

$$p(\zeta, t) = \begin{cases} \Delta p \left(1 - \dfrac{\zeta}{b}\right) + \Gamma \zeta \left(1 - \dfrac{V_T t}{b}\right) & \text{if } \quad 0 \leq \zeta \leq V_T t \\ (\Delta p + \Gamma V_T t) \left(1 - \dfrac{\zeta}{b}\right) & \text{if } \quad V_T t < \zeta \leq b \end{cases} \qquad \text{where } \Gamma = \frac{(\gamma_1 + \gamma_2) V_T \Delta T}{D}. \tag{24}$$

The p profile consists in two rectilinear segments with uniform gradients slowly varying with time, matching to each other continuously in $\zeta = V_T t$ (the thermal front, red line in Fig. 2b). Since q (the volumetric flow) is proportional to $\mathrm{d}p/\mathrm{d}\zeta$ (according to the Darcy law) the discontinuity of the pressure gradient can be ascribed to the density change due to the temperature discontinuity: the mass flow must be

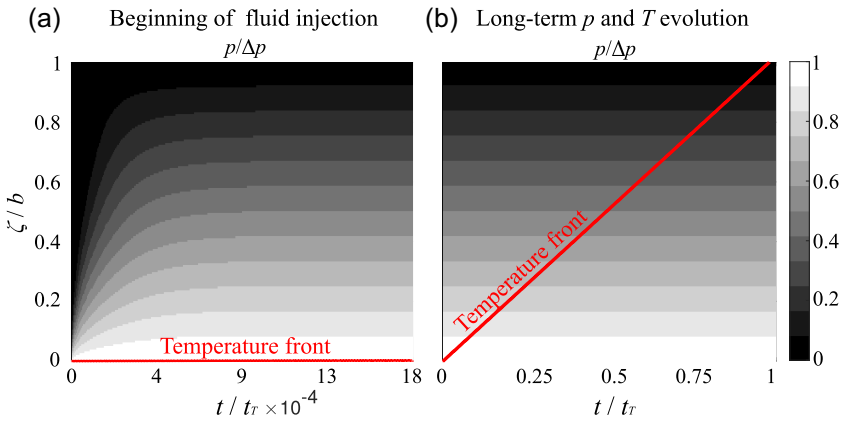

Figure 2. Evolution of p and T across the TPE thickness b. The pore pressure p rapidly attains a nearly uniform gradient, before the T front has advanced appreciably (a). Most of the T propagation takes place under a nearly constant pressure gradient (b). We assumed $\Delta p = 10$ MPa, $\Delta T = 100$ K, with material parameters pertinent to Berea sandstone (Rice & Cleary 1976).

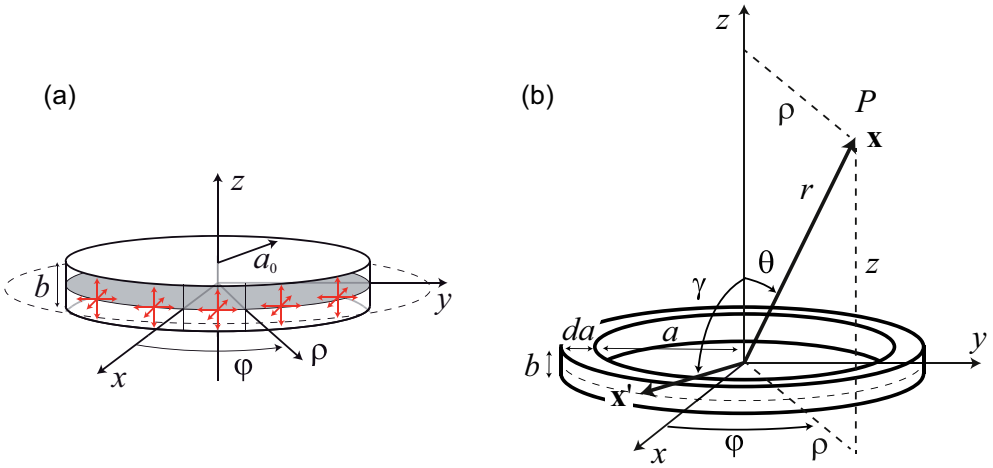

Figure 3. (a) TPE source due to increasing temperature T and pore pressure p within a flat disc with radius a_0 and thickness b embedded within an elastic unbounded medium. Red arrows represent three orthogonal force dipoles located in $\forall\, \mathbf{x}' \in V_S$ contributing to displacement in $\mathbf{x}$ through $\frac{\partial G_{ik}(\mathbf{x},\mathbf{x}')}{\partial x'_k}$ (eq. 7 in the main text). (b) Parameters used to compute the displacement potential $\mathrm{d}\Phi_R$ at a point P due to an elementary TPE ring with volume $\mathrm{d}V_s = 2\pi a b\, \mathrm{d}a$. Spherical (r, θ, φ) and cylindrical (ρ, φ, z) coordinates of P are indicated.

continuous, not the volumic flow. However, $\Gamma \ll \frac{\Delta p}{b}$ unless ΔT is unreasonably high: using TPE parameters pertinent to Berea sandstone, we get $\Gamma/\Delta T = 1.4 \times 10^{-4} \Delta p/b$: ΔT should be greater than 10^3 K in order to provide important changes to the pressure gradient. Thus, the two gradients may be safely assumed very close to the standard stationary value $\Delta p/b$ as shown in Fig. 2(b).

For a TPE disc located within a half-space, Nespoli *et al.* (2021) obtained the same eq. (19) assuming a configuration of uniaxial strain with constant vertical stress inside the inclusion. The latter restriction is no more needed in the present case, as in a full space $\epsilon_{kk} = \epsilon_1$, according to eq. (12) and the isotropic stress may be expressed in terms of T and p only. According to our results (eq. 21 and Fig. 2b) and the ones shown in fig. 2 of Nespoli *et al.* (2021), for each instant of time, a discontinuous vertical profile for the TPE potency ϵ_0 is obtained, as considered in the following Section 7.

5 DISC SHAPED TPE SOURCE

The TPE inclusion considered by Belardinelli *et al.* (2019) is a spherically symmetric TPE shell surrounding a spherical pressurized magma chamber. In this paper, we consider a more realistic shape for the TPE inclusion consisting in a flat cylinder with radius a_0 and small thickness $b \ll a_0$ (Fig. 3a).

The problem for the displacement field due to a thin TPE disc is formally similar to the gravitational field due to a galactic disc with uniform density (Villumsen 1983, 1985) or the electrostatic field due to a uniformly charged disc (Jackson 1999). However, no analogy with the mentioned problems may be suggested for the stress and strain fields within and outside a TPE source.

5.1 The potential field of a ring element

The TPE disc depicted in Fig. 3(a) is axially symmetric and V_S may be decomposed into infinitesimal annular rings over the plane $z = 0$ with radius a around the z-axis, as depicted in Fig. 3(b).

Even if cylindrical coordinates may seem a more natural coordinate system for discs, a solution in terms of spherical coordinates is much more easily implemented. The potential $\mathrm{d}\Phi_R$ generated at a point P with spherical coordinates r, θ, φ by an elementary TPE ring can be written as an expansion in Legendre polynomials $P_\ell(\cos\theta)$ (see e.g. Jackson 1999):

$$\mathrm{d}\Phi_R(r,\theta) = \begin{cases} \dfrac{\mathrm{d}V_s}{a}\displaystyle\sum_{\ell=0}^{\infty}\left(\frac{r}{a}\right)^{\ell} P_\ell(\cos\gamma)P_\ell(\cos\theta), & \text{if} \quad r < a \\ \dfrac{\mathrm{d}V_s}{r}\displaystyle\sum_{\ell=0}^{\infty}\left(\frac{a}{r}\right)^{\ell} P_\ell(\cos\gamma)P_\ell(\cos\theta), & \text{if} \quad r > a \end{cases}, \tag{25}$$

where $\mathrm{d}V_s = 2\pi a\, b\, \mathrm{d}a$ is the ring volume, a is the ring radius, $r = |\mathbf{x}|$, γ is the angle between the z-axis and any point $\mathbf{x}'$ of the ring and θ is the angle between the z-axis and the position vector $\mathbf{x}$ where $\mathrm{d}\Phi_R$ is computed. The disc is assumed to lay on the plane $z = 0$, so that $\gamma = \frac{\pi}{2}$ and $P_\ell(\cos\gamma) = P_\ell(0)$ for all the rings composing the disc.

If $\theta = 0$, the point $\mathbf{x}$ is on the z-axis and $\mathrm{d}\Phi_R$ may be computed by elementary methods from eq. (11) since $|\mathbf{x} - \mathbf{x}'| = \sqrt{r^2 + a^2}$ for all points in the ring and

$$\mathrm{d}\Phi_R(r, \theta = 0) = \frac{\mathrm{d}V_s}{\sqrt{r^2 + a^2}}. \tag{26}$$

Legendre polynomials $P_\ell(\cos\theta)$ are symmetric or anti-symmetric functions of $x = \cos\theta$, since $P_\ell(-x) = (-1)^\ell P_\ell(x)$; they are normalized to unity in $x = 1$ and their values are confined within ± 1, $\forall x \in [-1, 1]$ (see e.g. Abramowitz & Stegun 1965). Legendre polynomials may be efficiently computed using the recurrence relation

$$\ell P_\ell(x) = (2\ell - 1)x P_{\ell-1}(x) - (\ell - 1)P_{\ell-2}(x) \qquad \text{with } P_0(x) = 1 \text{ and } P_1(x) = x \tag{27}$$

Only even polynomials survive in eq. (25), since

$$c_\ell \equiv P_\ell(0) = \begin{cases} \frac{(-1)^m}{4^m}\frac{(2m)!}{(m!)^2} & \text{if} \quad \ell = 2m \\ 0 & \text{if} \quad \ell = 2m + 1 \end{cases} \qquad m = 0, 1, 2, \ldots \tag{28}$$

Coefficients $c_\ell = P_\ell(0)$ may be computed more conveniently from the recurrence relation (eq. 27):

$$\ell c_\ell = -(\ell - 1)c_{\ell-2} \qquad \text{with } c_0 = 1 \text{ and } c_1 = 0 \tag{29}$$

from which it is clear that odd terms vanish in eq. (25), while even coefficients are $c_{2m} = -\frac{2m-1}{2m}c_{2m-2}$, for example $c_0 = 1$, $c_2 = -\frac{1}{2}$, $c_4 = \frac{3}{8}$, $c_6 = -\frac{5}{16}$, ... Using Stirling's formula in eq. (28), we get

$$c_{2m} \sim \frac{(-1)^m}{(\pi m)^{1/2}} \qquad \text{(asymptotically, for large } m \text{ values)}. \tag{30}$$

The potential $\mathrm{d}\Phi_R$ due to one ring with radius a is then

$$\mathrm{d}\Phi_R(r,\theta) = \begin{cases} \mathrm{d}\Phi_R^{in}(r,\theta) = (2\pi b\, \mathrm{d}a)\displaystyle\sum_{m=0}^{\infty}\left(\frac{r}{a}\right)^{2m} c_{2m} P_{2m}(\cos\theta) & \text{if} \quad r \le a \\ \mathrm{d}\Phi_R^{ex}(r,\theta) = (2\pi b\, \mathrm{d}a)\displaystyle\sum_{m=0}^{\infty}\left(\frac{a}{r}\right)^{2m+1} c_{2m} P_{2m}(\cos\theta) & \text{if} \quad r \ge a \end{cases}. \tag{31}$$

We shall denote the region $r < a_0$ as the internal domain and the region $r > a_0$ as the external domain; the internal domain is a sphere with radius a_0 and it must not be confused with the TPE source region which is the thin disc (Fig. 3a).

5.2 The potential field of the thin disc

In order to compute the potential Φ_D, due to the entire disc, we superpose the potential $\mathrm{d}\Phi_R$ due to all rings with $0 \le a \le a_0$, integrating eq. (31) with respect to a from $a = 0$ to $a = a_0$:

$$\Phi_D(r,\theta) = \int_0^{a_0} \mathrm{d}\Phi_R(r,\theta) = \begin{cases} \displaystyle\int_0^r \mathrm{d}\Phi_R^{ex} + \int_r^{a_0} \mathrm{d}\Phi_R^{in} & \text{if} \quad r \le a_0 \\ \displaystyle\int_0^{a_0} \mathrm{d}\Phi_R^{ex} & \text{if} \quad r \ge a_0 \end{cases}. \tag{32}$$

Inserting eq. (31), the following result is obtained for $r < a_0$:

$$\begin{aligned}\Phi_D(r,\theta) &= (2\pi b)\sum_{m=0}^{\infty} c_{2m} P_{2m}(x)\left[\int_0^r \left(\frac{a}{r}\right)^{2m+1} \mathrm{d}a + \int_r^{a_0} \left(\frac{r}{a}\right)^{2m} \mathrm{d}a\right] \quad \text{if} \quad r < a_0 \\ &= (2\pi b a_0)\sum_{m=0}^{\infty} c_{2m} P_{2m}(x)\left[\left(\frac{1}{2m+2}+\frac{1}{2m-1}\right)\frac{r}{a_0} - \frac{1}{2m-1}\left(\frac{r}{a_0}\right)^{2m}\right],\end{aligned} \tag{33}$$

where $x = \cos\theta$. Similarly, if $r > a_0$, we obtain:

$$\Phi_D(r,\theta) = (2\pi b a_0)\sum_{m=0}^{\infty} \frac{c_{2m}}{2m+2} P_{2m}(x)\left(\frac{a_0}{r}\right)^{2m+1} \quad \text{if} \quad r > a_0. \tag{34}$$

In particular, if $r = 0$, only the term $m = 0$ survives in eqs (33) and $\Phi_D(0,\theta) = (2\pi b a_0)$.

Along the symmetry axis, $r = z$ and $\theta = 0$, if $z > 0$, while $r = -z$ and $\theta = \pi$, if $z < 0$; we may compute directly Φ_D from eq. (26), obtaining

$$\Phi_D(r = |z|, \rho = 0) = 2\pi b \int_0^{a_0} \frac{a}{\sqrt{r^2+a^2}}\mathrm{d}a = 2\pi b a_0\left[\sqrt{\frac{r^2}{a_0^2}+1} - \frac{r}{a_0}\right] \tag{35}$$

that can be used to test the convergence of the expansions (33) and (34) which is very slow when r is close to a_0.

5.3 The displacement field of the thin disc

Using spherical coordinates (r, θ, φ), we have

$$\nabla\Phi = \left(\frac{\partial\Phi}{\partial r}, \frac{1}{r}\frac{\partial\Phi}{\partial\theta}, \frac{1}{r\sin\theta}\frac{\partial\Phi}{\partial\varphi}\right); \tag{36}$$

then, the displacement component u_φ vanishes identically, as might be anticipated from symmetry considerations. Non-vanishing components u_r, u_θ can be written from eqs (33) and (34) according to eq. (10) using the dimensionless constant

$$A = \epsilon_1 \frac{b}{2a_0}, \tag{37}$$

where ϵ_1 linearly depends on the TPE inclusion potency ϵ_0 (see eq. 11).

We have

$$u_r(r,\theta) = -Aa_0\sum_{m=0}^{\infty} c_{2m} P_{2m}(x)\left[\left(\frac{1}{2m+2}+\frac{1}{2m-1}\right) - \frac{2m}{2m-1}\left(\frac{r}{a_0}\right)^{2m-1}\right] \quad \text{if} \quad r < a_0 \tag{38}$$

$$u_r(r,\theta) = Aa_0\sum_{m=0}^{\infty} c_{2m} P_{2m}(x)\frac{2m+1}{2m+2}\left(\frac{a_0}{r}\right)^{2m+2} \quad \text{if} \quad r > a_0 \tag{39}$$

Taking into account that $P_0(x) = 1$, the polar component of displacement is

$$u_\theta(r,\theta) = -Aa_0\sum_{m=1}^{\infty} c_{2m}\frac{\mathrm{d}P_{2m}(x)}{\mathrm{d}\theta}\left[\left(\frac{1}{2m+2}+\frac{1}{2m-1}\right) - \frac{1}{2m-1}\left(\frac{r}{a_0}\right)^{2m-1}\right] \quad \text{if} \quad r < a_0 \tag{40}$$

$$u_\theta(r,\theta) = -Aa_0\sum_{m=1}^{\infty} c_{2m}\frac{\mathrm{d}P_{2m}(x)}{\mathrm{d}\theta}\left[\frac{1}{2m+2}\left(\frac{a_0}{r}\right)^{2m+2}\right] \quad \text{if} \quad r > a_0 \tag{41}$$

and the differential relation

$$\frac{\mathrm{d}P_{\ell+1}(x)}{\mathrm{d}x} = (\ell+1)P_\ell(x) + x\frac{\mathrm{d}P_\ell(x)}{\mathrm{d}x}, \quad \text{with } x = \cos\theta \tag{42}$$

may be used to compute iteratively $\frac{\mathrm{d}P_{2m}(x)}{\mathrm{d}\theta}$. We may easily check from eqs (38) and (39) and from eqs (40) and (41) that both the displacement components u_r and u_θ are continuous term by term in $r = a_0$; however, this is not sufficient to guarantee that the sum of the series is continuous in $r = a_0$ on the disc plane ($\theta = \pi/2$), as explained in detail in the Appendix.

From eq. (35) we obtain the closed form solution along the z-axis (where $\theta = 0, \pi$)

$$\begin{aligned}u_r(r = z, \theta = 0) &= Aa_0\left(1 - \frac{r}{\sqrt{r^2+a_0^2}}\right) = u_z(z > 0, \rho = 0) \\ u_r(r = -z, \theta = \pi) &= Aa_0\left(1 - \frac{r}{\sqrt{r^2+a_0^2}}\right) = -u_z(z < 0, \rho = 0)\end{aligned}, \tag{43}$$

where z, ρ are cylindrical coordinates: $z = r\cos\theta$ and $\rho = r\sin\theta$ (see Fig. 3a). Of course, u_θ must vanish along the z-axis and actually all terms vanish in the expansions (40) and (41) since $\frac{\mathrm{d}P_{2m}(x)}{\mathrm{d}\theta} = -\sin\theta\frac{\mathrm{d}P_{2m}(x)}{\mathrm{d}x}$. Figs 4 and 5 show u_r and u_θ versus r and versus θ, respectively.

When $r = 0$, we have

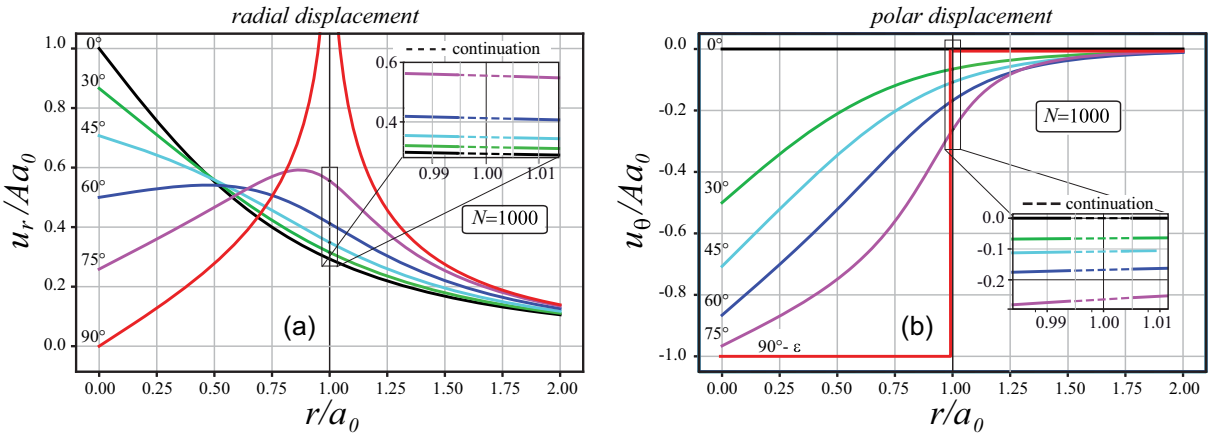

Figure 4. Normalized displacement components u_r/Aa_0, u_θ/Aa_0 versus r/a_0 around a thin circular disc for a few values of θ between 0° and 90°, using series truncation to order $N = 1000$. Displacements for $\theta \in [90°, 180°]$ may be obtained considering that u_r is an even function of $x = \cos\theta$ and u_θ is odd. Dotted segments in the inset show interpolated values between $r_1/a_0 = 0.995$ and $r_2/a_0 = 1.005$.

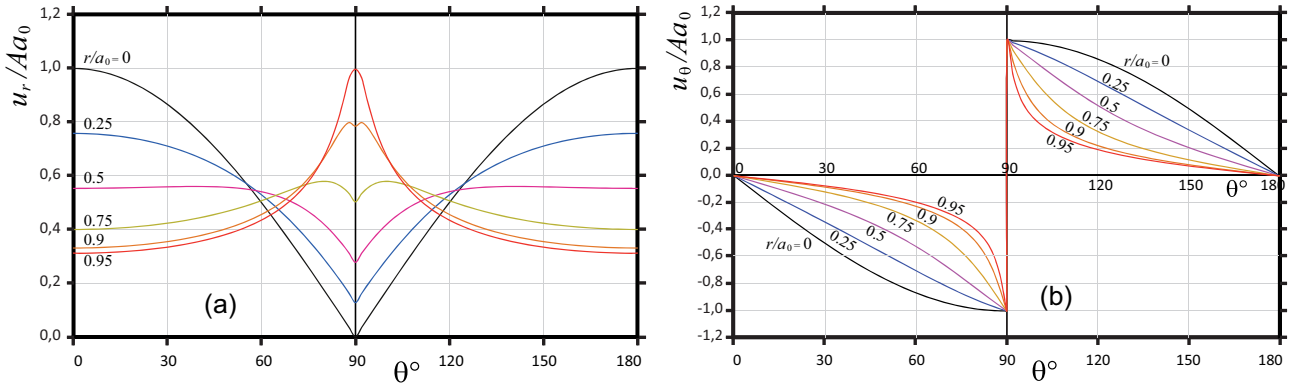

Figure 5. Displacement components u_r, u_θ versus θ around a thin circular disc for a few values of r/a_0 between 0 and 1, using series truncation to order $N = 80$. As discussed in the text, u_r is a continuous even function of $x = \cos\theta$ and u_θ is discontinuous and odd. In the external domain $r/a_0 > 1$ both displacement components are continuous and decrease rapidly (not shown to avoid confusion).

$$u_r(0,\theta) = -Aa_0 \sum_{m=0}^{\infty} c_{2m} P_{2m}(x) \left[\frac{1}{2m+2} + \frac{1}{2m-1}\right] \tag{44}$$

$$u_\theta(0,\theta) = -Aa_0 \sum_{m=1}^{\infty} c_{2m} \frac{\mathrm{d}P_{2m}(x)}{\mathrm{d}\theta} \left[\left(\frac{1}{2m+2} + \frac{1}{2m-1}\right)\right]. \tag{45}$$

From symmetry considerations, the displacement vector **u** must be directed along z when $r \to 0$ and eq. (43) yields $u_z = Aa_0$ in $z = 0^+$, where $x = \cos\theta = 0^+$, while $u_z = -Aa_0$ in $z = 0^-$, where $x = \cos\theta = 0^-$. Accordingly, when $r \to 0$, $\mathbf{u} \simeq Aa_0 \hat{\mathbf{k}}\,\mathrm{sgn}(x)$, where $\hat{\mathbf{k}} = (\cos\theta\,\hat{\mathbf{e}}_r - \sin\theta\,\hat{\mathbf{e}}_\theta)$ is the unit vector along the z-axis, $\hat{\mathbf{e}}_r$, $\hat{\mathbf{e}}_\theta$ are unit vectors in the radial and polar directions and $\mathrm{sgn}(x) = 1$ if $x > 0$, $\mathrm{sgn}(x) = -1$ if $x < 0$. In spherical coordinates we have $u_r(0,\theta) = Aa_0|\cos\theta|$ and $u_\theta(0,\theta) = -Aa_0\,\mathrm{sgn}(\cos\theta)\sin\theta$, with a jump discontinuity in $\theta = \pi/2$. We conclude that

$$-\sum_{m=0}^{\infty} c_{2m} P_{2m}(x) \left[\frac{1}{2m+2} + \frac{1}{2m-1}\right] = |\cos\theta| = |x| \tag{46}$$

$$\sum_{m=1}^{\infty} c_{2m} \frac{\mathrm{d}P_{2m}(x)}{\mathrm{d}\theta} \left[\frac{1}{2m+2} + \frac{1}{2m-1}\right] = \mathrm{sgn}(\cos\theta)\sin\theta = \mathrm{sgn}(x)\sqrt{1-x^2}. \tag{47}$$

From Fig. 6 we see that convergence is fast for the series (eq. 46) but much slower for (eq. 47), as it typically happens in the expansion of a function containing a jump discontinuity. Taking into account the previous considerations we may rewrite:

$$\Phi_D(r,\theta) = (2\pi b a_0)\left\{1 - |x|\left(\frac{r}{a_0}\right) - \sum_{m=1}^{\infty} c_{2m} P_{2m}(x) \frac{1}{2m-1}\left(\frac{r}{a_0}\right)^{2m}\right\} \quad \text{if} \quad r < a_0 \tag{48}$$

$$u_r(r,\theta) = Aa_0\left\{|x| + \sum_{m=1}^{\infty} c_{2m} P_{2m}(x) \frac{2m}{2m-1}\left(\frac{r}{a_0}\right)^{2m-1}\right\} \quad \text{if} \quad r < a_0 \tag{49}$$

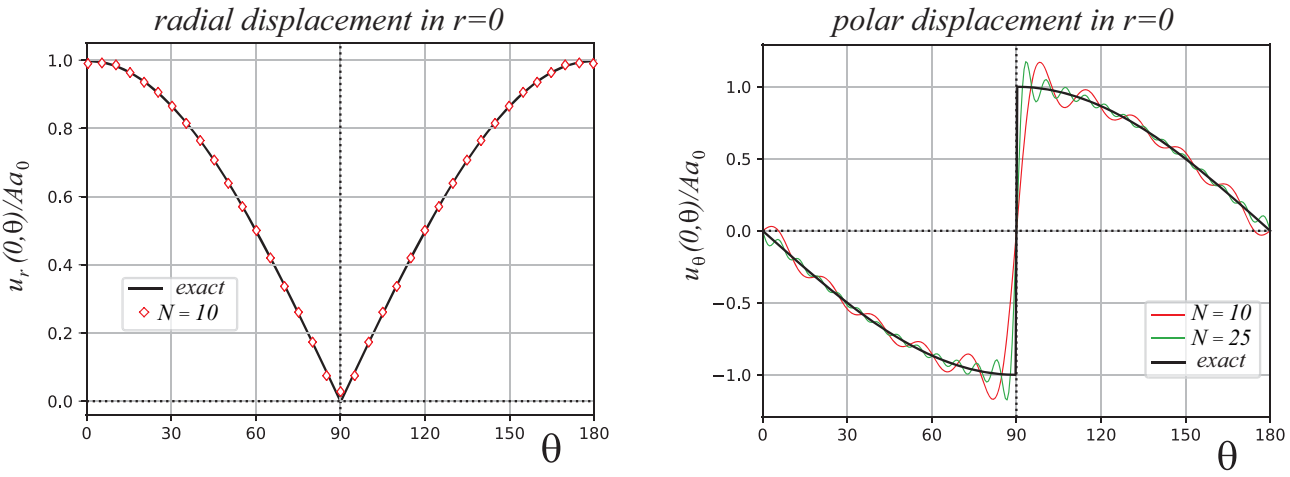

Figure 6. Displacement components u_r/Aa_0 and u_θ/Aa_0 computed in $r = 0$ according to the series expansion truncated at order N (indicated in the box) compared with the exact solution provided by eqs (46) and (47).

and

$$u_\theta(r,\theta) = -Aa_0 \left\{ \operatorname{sgn}(x)\sin\theta - \sum_{m=1}^{\infty} c_{2m} \frac{\mathrm{d}P_{2m}(x)}{\mathrm{d}\theta} \frac{1}{2m-1} \left(\frac{r}{a_0}\right)^{2m-1} \right\} \quad \text{if} \quad r < a_0. \tag{50}$$

The previous solutions for the displacement field have several similarities with a mode-I Volterra dislocation (e.g. Aki & Richards 2002) characterized by uniform opening along z, but the equivalent body forces are described by a different moment tensor: isotropic for the TPE disc, as shown by eq. (7), with a strong deviatoric component for a mode-I Volterra dislocation. This difference has important implications for the stress and strain field inside the TPE inclusion, as we will see in the following sections. For $r < a_0$, the strain components are derived from eqs (49) and (50) in the next section.

5.4 The strain tensor field of the thin disc

In spherical coordinates, the strain tensor components are given by:

$$\begin{aligned} &\epsilon_{rr} = \tfrac{\partial u_r}{\partial r}, && \epsilon_{\theta\theta} = \tfrac{1}{r}\left(\tfrac{\partial u_\theta}{\partial \theta} + u_r\right), && \epsilon_{\varphi\varphi} = \tfrac{1}{r\sin\theta}\left(\tfrac{\partial u_\varphi}{\partial \varphi} + u_r\sin\theta + u_\theta\cos\theta\right) \\ &\epsilon_{r\theta} = \tfrac{1}{2}\left(\tfrac{1}{r}\tfrac{\partial u_r}{\partial \theta} + \tfrac{\partial u_\theta}{\partial r} - \tfrac{u_\theta}{r}\right), && \epsilon_{r\varphi} = \tfrac{1}{2}\left(\tfrac{1}{r\sin\theta}\tfrac{\partial u_r}{\partial \varphi} + \tfrac{\partial u_\varphi}{\partial r} - \tfrac{u_\varphi}{r}\right), && \epsilon_{\theta\varphi} = \tfrac{1}{2r}\left(\tfrac{1}{\sin\theta}\tfrac{\partial u_\theta}{\partial \varphi} + \tfrac{\partial u_\varphi}{\partial \theta} - u_\varphi\cot\theta\right) \end{aligned} \tag{51}$$

In the following, we rewrite $u_{rr} = \frac{\partial u_r}{\partial r}$, $u_{r\theta} = \frac{\partial u_r}{\partial \theta}$, $u_{\theta\theta} = \frac{\partial u_\theta}{\partial \theta}$, $u_{\theta r} = \frac{\partial u_\theta}{\partial r}$. Taking into account that in the present problem $u_\varphi = 0$, that u_r, u_θ are independent of φ and that, from eqs (10) and (36), $u_{\theta r} = \frac{1}{r}(u_{r\theta} - u_\theta)$, we have

$$\begin{aligned} &\epsilon_{rr} = u_{rr}, \ \epsilon_{\theta\theta} = \frac{1}{r}(u_{\theta\theta} + u_r), \ \epsilon_{\varphi\varphi} = \frac{1}{r\sin\theta}(u_r\sin\theta + u_\theta\cos\theta) \\ &\epsilon_{r\theta} = u_{\theta r}, \ \epsilon_{r\varphi} = 0, \qquad\qquad \epsilon_{\theta\varphi} = 0 \end{aligned}. \tag{52}$$

By straightforward calculation we get the following explicit expressions:

5.4.1 Radial component

$$\epsilon_{rr} = A\sum_{m=1}^{\infty} 2mc_{2m}P_{2m}(x)\left[\frac{r}{a_0}\right]^{2m-2} \quad \text{if} \quad r < a_0 \tag{53}$$

$$\epsilon_{rr} = -A\sum_{m=0}^{\infty}(2m+1)c_{2m}P_{2m}(x)\left[\frac{a_0}{r}\right]^{2m+3} \quad \text{if} \quad r > a_0 \tag{54}$$

If $\theta = 0$, that is $x = 1$, from eq. (43) we have the closed form result

$$\epsilon_{rr}(r,\theta=0) = -A\left(1+\frac{r^2}{a_0^2}\right)^{-3/2} \tag{55}$$

The series (eqs 53 and 54) are absolutely convergent if $r \neq a_0$ but clearly are not convergent when $r = a_0$, where analytic continuation may be used if $\theta \neq \frac{\pi}{2}$; if $\theta = \frac{\pi}{2}$, the series diverge to $\pm\infty$ (Fig. 7a).

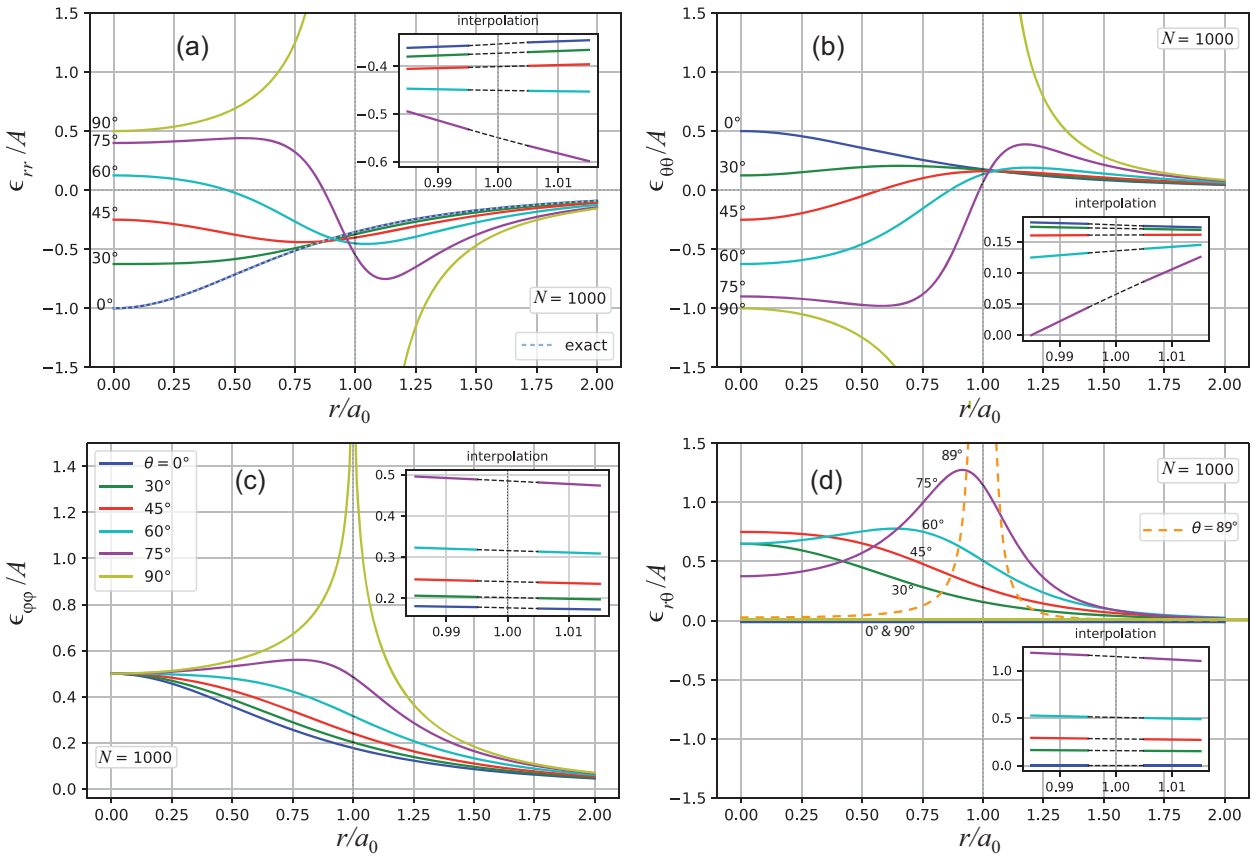

Figure 7. Strain components ϵ_{ij}/A versus r/a_0 around a thin circular disc for a few values of θ between 0° and 90°. Trends for $90° < \theta \leq 180°$ may be simply obtained considering that ϵ_{rr}, $\epsilon_{\theta\theta}$, $\epsilon_{\varphi\varphi}$ are even functions of $x = \cos\theta$ while $\epsilon_{r\theta}$ is odd.

5.4.2 Polar component

The normal strain component in the polar direction is

$$\epsilon_{\theta\theta} = A\left\{2\delta(x)\frac{a_0}{r} + \sum_{m=1}^{\infty}\frac{c_{2m}}{2m-1}\left(\frac{r}{a_0}\right)^{2m-2}\left[\frac{d^2P_{2m}}{\mathrm{d}\theta^2} + 2mP_{2m}\right]\right\} \quad \text{if} \quad (r < a_0) \tag{56}$$

$$\epsilon_{\theta\theta} = A\left\{\frac{1}{2}\left(\frac{a_0}{r}\right)^3 + \sum_{m=1}^{\infty}\frac{c_{2m}}{2m+2}\left(\frac{a_0}{r}\right)^{2m+3}\left[(2m+1)P_{2m} - \frac{d^2P_{2m}}{\mathrm{d}\theta^2}\right]\right\} \quad \text{if} \quad (r > a_0) \tag{57}$$

where $\delta(x)$ is Dirac's delta, which arises from the derivative of $\mathrm{sgn}(x)$ in eq. (50).

The second derivative of $d^2P_n(x)/\mathrm{d}\theta^2$ may be conveniently rewritten using the differential equation obeyed by Legendre polynomials

$$(1-x^2)\frac{d^2P_n(x)}{\mathrm{d}x^2} - 2x\frac{\mathrm{d}P_n(x)}{\mathrm{d}x} + n(n+1)P_n(x) = 0, \qquad \text{with } x = \cos\theta. \tag{58}$$

We have:

$$\frac{d^2P_{2m}(\cos\theta)}{\mathrm{d}\theta^2} = xP'_{2m}(x) - 2m(2m+1)P_{2m}(x), \tag{59}$$

where P' denotes the first derivative of P with respect to $x = \cos\theta$ and the differential relation (42) may be used to compute $P'_{2m}(x)$. In the disc plane we have $\theta = \frac{\pi}{2}$ and $x = 0$ so that

$$\left.\frac{d^2P_{2m}(\cos\theta)}{\mathrm{d}\theta^2}\right|_{\theta=\pi/2} = -2m(2m+1)c_{2m} \tag{60}$$

Thus, the infinite series (eqs 56 and 57) are not convergent in $r = a_0$, where analytical continuation may be used if $\theta \neq \frac{\pi}{2}$ and diverge to $\mp\infty$ in $r = a_0$ if $\theta = \frac{\pi}{2}$ (Fig. 7b).

5.4.3 Azimuthal component

The azimuthal normal component is

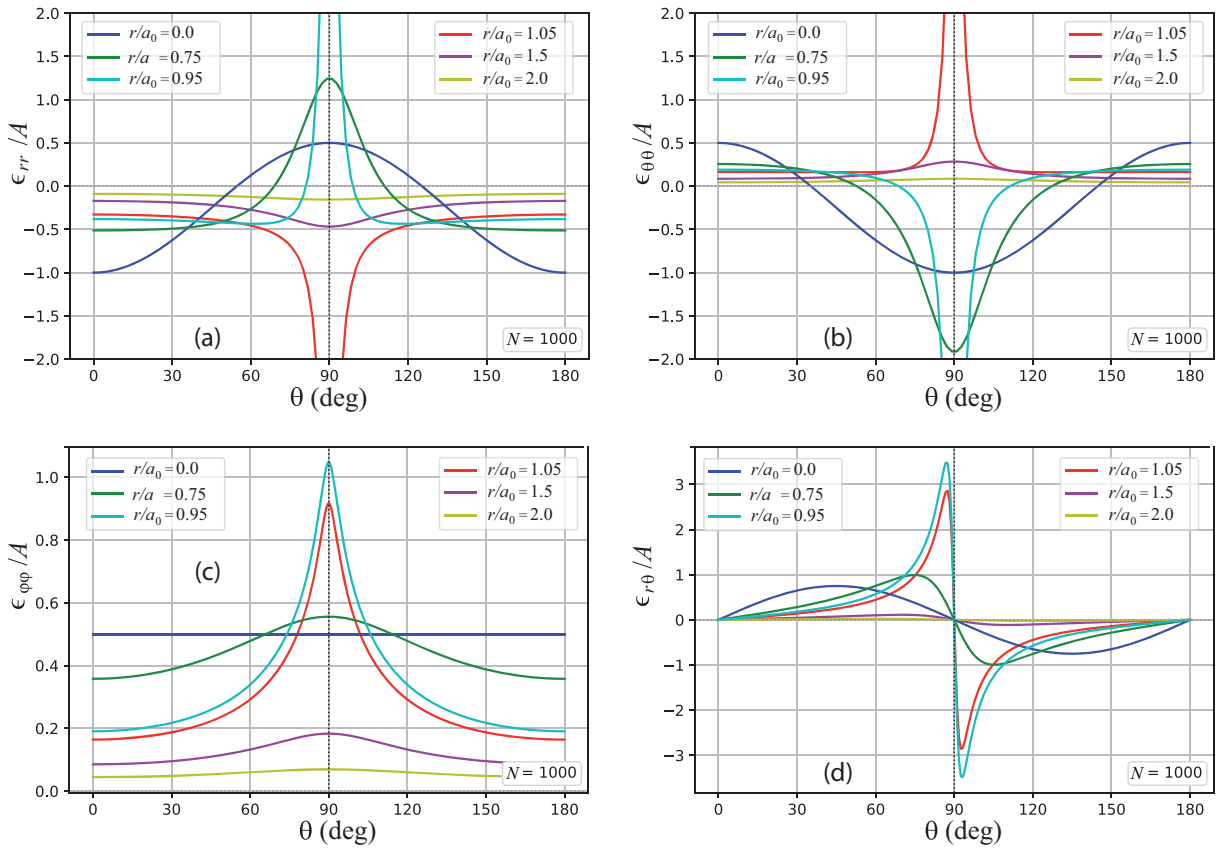

Figure 8. Strain components ϵ_{ij}/A versus θ around a thin circular disc for a few values of r.

$$\epsilon_{\varphi\varphi} = A\sum_{m=1}^{\infty}\frac{c_{2m}}{2m-1}\left(\frac{r}{a_0}\right)^{2m-2}\left[2m\,P_{2m}+\frac{\cos\theta}{\sin\theta}\frac{\mathrm{d}P_{2m}}{\mathrm{d}\theta}\right] \qquad \text{if} \quad r < a_0. \tag{61}$$

$$\epsilon_{\varphi\varphi} = A\sum_{m=0}^{\infty}\frac{c_{2m}}{2m+2}\left(\frac{a_0}{r}\right)^{2m+3}\left[(2m+1)P_{2m}-\frac{\cos\theta}{\sin\theta}\frac{\mathrm{d}P_{2m}}{\mathrm{d}\theta}\right] \qquad \text{if} \quad r > a_0. \tag{62}$$

Again, these series are not convergent in $r = a_0,\ \theta \neq \frac{\pi}{2}$, where analytical continuation should be used and diverge to $+\infty$ in $r = a_0,\ \theta = \frac{\pi}{2}$ (Fig. 7c).

5.4.4 Shear component

The only non-vanishing shear component of strain is

$$\epsilon_{r\theta} = A\sum_{m=1}^{\infty}c_{2m}\frac{\mathrm{d}P_{2m}}{\mathrm{d}\theta}\left(\frac{r}{a_0}\right)^{2m-2} \qquad \text{if} \quad (r < a_0) \tag{63}$$

$$\epsilon_{r\theta} = A\sum_{m=1}^{\infty}c_{2m}\frac{\mathrm{d}P_{2m}}{\mathrm{d}\theta}\left(\frac{a_0}{r}\right)^{2m+3} \qquad \text{if} \quad (r > a_0). \tag{64}$$

These series are absolutely convergent if $r \neq a_0$ and are not convergent if $r = a_0$, where analytical continuation may be used if $\theta \neq \frac{\pi}{2}$ (Fig. 7d). If $\theta = \frac{\pi}{2}$, $\epsilon_{r\theta}$ vanishes changing sign across the disc section. It is worth to note that if $\theta = \frac{\pi}{2}$ a singular term $= Aa_0\mathrm{sgn}(x)\delta(r - a_0)$ should be added to eqs (63) and (64) due to the sudden change of u_θ for $\theta = \frac{\pi}{2}^{\mp}$ from $\mp Aa_0$ if $r < a_0$ to zero if $r > a_0$. This jump is responsible for a localized peak of $\epsilon_{r\theta}$ near $r = a_0$ when θ is only slightly different from 90° (dashed line).

All strain components are shown graphically in Fig. 7 as functions of r and in Fig. 8 as functions of θ.

If $r < a_0$ and $x = \cos\theta \neq 0$ or if $r > a_0\ \forall x \in [-1, 1]$, using the differential eq. (58), we may easily check that $\epsilon_{rr} + \epsilon_{\theta\theta} + \epsilon_{\varphi\varphi} = 0$, outside the disc plane, as requested by eq. (12). In the interior of the TPE disc we must account for the effect of the δ-function appearing in eq. (56). We must also take into account the constraints imposed by the welded-boundary conditions on Σ, as we will see in the following section.

6 THE THIN DISC IN CYLINDRICAL COORDINATES

For geophysical applications, the deformation field within and close to the TPE disc of infinitesimal thickness, b, is best understood in cylindrical coordinates, if we assume that the disc symmetry axis, z, is the vertical direction. The transformation from spherical components u_r, u_θ, u_φ to cylindrical components u_z, u_ρ, u_φ preserves the right handed coordinate system. For a vector $\mathbf{u}$ we have

$$\begin{bmatrix} u_z \\ u_\rho \\ u_\varphi \end{bmatrix} = \begin{bmatrix} \cos\theta & -\sin\theta & 0 \\ \sin\theta & \cos\theta & 0 \\ 0 & 0 & 1 \end{bmatrix} \times \begin{bmatrix} u_r \\ u_\theta \\ u_\varphi \end{bmatrix}. \tag{65}$$

We note that u_φ is left unchanged. For the strain tensor ϵ_{ij} we have

$$\begin{bmatrix} \epsilon_{zz} & \epsilon_{z\rho} & \epsilon_{z\varphi} \\ \epsilon_{\rho z} & \epsilon_{\rho\rho} & \epsilon_{\rho\varphi} \\ \epsilon_{\varphi z} & \epsilon_{\varphi\rho} & \epsilon_{\varphi\varphi} \end{bmatrix} = \begin{bmatrix} \cos\theta & -\sin\theta & 0 \\ \sin\theta & \cos\theta & 0 \\ 0 & 0 & 1 \end{bmatrix} \times \begin{bmatrix} \epsilon_{rr} & \epsilon_{r\theta} & \epsilon_{r\varphi} \\ \epsilon_{\theta r} & \epsilon_{\theta\theta} & \epsilon_{\theta\varphi} \\ \epsilon_{\varphi r} & \epsilon_{\varphi\theta} & \epsilon_{\varphi\varphi} \end{bmatrix} \times \begin{bmatrix} \cos\theta & \sin\theta & 0 \\ -\sin\theta & \cos\theta & 0 \\ 0 & 0 & 1 \end{bmatrix}, \tag{66}$$

where the product between matrices is the usual product 'rows times columns'. In particular, over the top and bottom surfaces of the disc ($z = \pm\frac{b}{2}$), we have, respectively, $\theta = \frac{\pi}{2}^{\mp}$ and $u_z = -u_\theta$, $u_\rho = u_r$ while $\epsilon_{zz} = \epsilon_{\theta\theta}, \epsilon_{z\rho} = -\epsilon_{r\theta}, \epsilon_{\rho\rho} = \epsilon_{rr}$.

The 'welded boundary conditions' over the top and bottom disc faces (i.e. over $z = \pm\frac{b}{2}, \forall\rho < a_0$) require continuity of displacements u_z, u_ρ and continuity of tractions $\tau_{\rho z}$, τ_{zz} going from the interior ($|z| < \frac{b}{2}$) to the exterior ($|z| > \frac{b}{2}$) of the disc. If $\theta = \frac{\pi}{2}$, we get from eq. (52) $\epsilon_{\varphi\varphi} = u_r/r = u_\rho/\rho$ so that even $\epsilon_{\varphi\varphi}$ must be continuous across the top and bottom disc faces. Continuity of u_ρ finally requires that $\epsilon_{\rho\rho} = \partial u_\rho/\partial\rho$ is continuous over the disc faces. Considering the infinitesimal thickness of the disc, u_ρ, $\epsilon_{\rho\rho}$, $\epsilon_{\varphi\varphi}$ within the source region are given, respectively, by eqs (49), (53) and (61) with $x = \cos\theta = 0$. When $\theta = \frac{\pi}{2}$ the shear component $\epsilon_{z\rho} = -\epsilon_{r\theta}$ vanishes according to eq. (63).

As stated after eq. (13), a finite amplitude discontinuity is present in ϵ_{zz} across the top and bottom faces of the disc: thus, the value of ϵ_{zz} above the top surface and below the bottom surface of the disc may be computed either from eq. (56) in the limit $x = 0^{\mp}$, so that the δ-function vanishes, or from $\epsilon_{kk} = 0$ (eq. 12), which yields $\epsilon_{zz} = -(\epsilon_{\rho\rho} + \epsilon_{\varphi\varphi})$. Within the source region, $\epsilon_{kk} = \epsilon_1$ (from eq. 12) so that $\epsilon_{zz} = \epsilon_1 - (\epsilon_{\rho\rho} + \epsilon_{\varphi\varphi})$. The addition of ϵ_1 in ϵ_{zz} within the source region may be understood from eq. (50) as due to the jump of u_z from $-Aa_0$ in $z = -\frac{b}{2}$ to $+Aa_0$ in $z = +\frac{b}{2}$. We may approximate to first order the singular term of u_z within the source region as $u_z^{\rm si} = 2Aa_0\frac{z}{b}$ so that $\epsilon_{zz}^{\rm si} = \frac{\partial u_z^{\rm si}}{\partial z} = 2\frac{A}{b}a_0 = \epsilon_1$, after inserting eq. (37). The same result for the singular component of strain, $\epsilon_{zz}^{\rm si}$, is obtained if the term containing the Dirac's δ-function in eq. (56) is approximated as

$$\epsilon_{zz}^{\rm si} = 2A\delta(x)\frac{a_0}{r} = 2A\delta\left(\frac{z}{r}\right)\frac{a_0}{r} = 2Aa_0\delta(z) \simeq \begin{cases} 2Aa_0\frac{1}{b} = \epsilon_1 & \text{if} \quad |z| \le \frac{b}{2} \\ 0 \quad \text{if} \quad |z| > \frac{b}{2} \end{cases} \tag{67}$$

according to the properties of the δ-function.

In analogy with the potential, we use the superscripts $^{(el)}$ and $^{(S)}$ to denote a tensorial field as evaluated outside and inside the disc, respectively. For $\rho < a_0$ the strain tensor $\epsilon_{ij}^{(el)}$ just above $z = b/2$ and below $z = -b/2$, that is $z \to 0^{\mp}$, and in $z = 0$, within the disc, $\epsilon_{ij}^{(S)}$ is provided by the following expressions after assuming $A = \epsilon_1\frac{b}{2a_0}$, $\theta = \frac{\pi}{2}$ and $r = \rho$ in eqs (53), (56) and (61)

$$\begin{aligned}
\epsilon_{\rho\rho}^{(S)}(\rho) &= \epsilon_{\rho\rho}(z = 0, \rho < a_0) = \epsilon_1\frac{b}{2a_0}\sum_{m=1}^{\infty} 2mc_{2m}^2\left[\frac{\rho}{a_0}\right]^{2m-2}, \\
\epsilon_{\varphi\varphi}^{(S)}(\rho) &= \epsilon_{\varphi\varphi}(z = 0, \rho < a_0) = \epsilon_1\frac{b}{2a_0}\sum_{m=1}^{\infty}\frac{2m}{2m-1}c_{2m}^2\left(\frac{\rho}{a_0}\right)^{2m-2}, \\
\epsilon_{zz}^{(S)}(\rho) &= \epsilon_{zz}(z = 0, \rho < a_0) = \epsilon_1 - (\epsilon_{\rho\rho} + \epsilon_{\varphi\varphi}) = \epsilon_1\left[1 - \frac{b}{2a_0}\sum_{m=1}^{\infty}\frac{4m^2}{2m-1}c_{2m}^2\left(\frac{\rho}{a_0}\right)^{2m-2}\right],
\end{aligned} \tag{68}$$

$$\begin{aligned}
&\epsilon_{\rho\rho}^{(el)}(z = 0^{\mp}, \rho < a_0) = \epsilon_{\rho\rho}^{(S)}(\rho), \\
&\epsilon_{\varphi\varphi}^{(el)}(z = 0^{\mp}, \rho < a_0) = \epsilon_{\varphi\varphi}^{(S)}(\rho), \\
&\epsilon_{zz}^{(el)}(z = 0^{\mp}, \rho < a_0) = -(\epsilon_{\rho\rho} + \epsilon_{\varphi\varphi}) = \epsilon_{zz}^{(S)}(\rho) - \epsilon_1,
\end{aligned}$$

while other components vanish.

Laterally outside the disc, that is for $\rho > a_0$ and $z = 0$, $\epsilon_{\rho\rho}^{(el)}$, $\epsilon_{zz}^{(el)}$ and $\epsilon_{\varphi\varphi}^{(el)}$ are given by eqs (54), (57) and (62), respectively with $x = 0$, that is $\theta = \frac{\pi}{2}$.

From eq. (3), the stress tensor out of the TPE disc (where both ϵ_{kk} and ϵ_0 vanish) is purely deviatoric so that we get simply

$$\tau_{\rho\rho}^{(el)} = 2\mu\epsilon_{\rho\rho}^{(el)}, \quad \tau_{\varphi\varphi}^{(el)} = 2\mu\epsilon_{\varphi\varphi}^{(el)}, \quad \tau_{zz}^{(el)} = 2\mu\epsilon_{zz}^{(el)}. \tag{69}$$

The stress tensor $\tau_{ij}^{(S)}$ within the TPE source is most easily computed after separating it into the isotropic component $\frac{1}{3}\tau_{kk}^{(S)}\delta_{ij}$ and the deviatoric component $\tau_{ij}^{(D)} = \tau_{ij}^{(S)} - \frac{1}{3}\tau_{kk}^{(S)}\delta_{ij}$; from the constitutive relation (3), taking into account that $\epsilon_1 = \frac{1+\nu}{1-\nu}\epsilon_0$, we get

$$\frac{1}{3}\tau_{kk}^{(S)}\delta_{ij} = -\frac{4}{3}\mu\epsilon_1\delta_{ij}, \qquad \tau_{ij}^{(D)} = 2\mu\epsilon_{ij}^{(D)} = 2\mu\left(\epsilon_{ij}^{(S)} - \frac{1}{3}\epsilon_1\delta_{ij}\right) \tag{70}$$

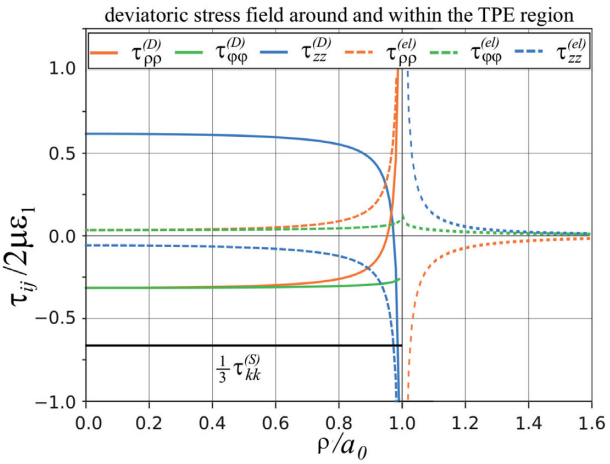

Figure 9. Deviatoric stress components, (normalized to $2\mu\epsilon_1$) within a TPE disc, computed at $z = 0^{\mp}$, with aspect ratio $b/a_0 = 1/10$ (solid lines) and just above or below the disc faces (dashed). The isotropic stress within the disc $\frac{1}{3}\tau_{kk}^{(S)}$ is also shown as the black solid line (τ_{kk} vanishes outside the TPE disc).

where $\epsilon_{ij}^{(D)} = \epsilon_{ij}^{(S)} - \frac{1}{3}\epsilon_{kk}^{(S)}\delta_{ij}$ is the deviatoric strain tensor.

In order to avoid cumbersome notation, the superscript (S) is omitted in the deviatoric strain and stress components inside the TPE source. The deviatoric stress components $\tau_{ij}^{(D)} = 2\mu\epsilon_{ij}^{(D)}$ within the TPE disc are

$$\begin{aligned}\tau_{\rho\rho}^{(D)} &= 2\mu\left(\epsilon_{\rho\rho} - \tfrac{1}{3}\epsilon_1\right)\\ \tau_{\varphi\varphi}^{(D)} &= 2\mu\left(\epsilon_{\varphi\varphi} - \tfrac{1}{3}\epsilon_1\right)\\ \tau_{zz}^{(D)} &= 2\mu\left(\epsilon_{zz} - \tfrac{1}{3}\epsilon_1\right) = 2\mu\left[\tfrac{2}{3}\epsilon_1 - (\epsilon_{\rho\rho} + \epsilon_{\varphi\varphi})\right].\end{aligned} \tag{71}$$

In Fig. 9 solid lines show the deviatoric components of stress within the TPE disc (normalized to $2\mu\epsilon_1$) assuming $b/a_0 = 1/10$ and dashed lines show the deviatoric components of stress just above the top surface of the disc (or just below the bottom surface). It is worth to recall that within a mode-I Volterra dislocation both stress and strain cannot be evaluated, since no material is present in the dislocation interior. Instead eq. (70) show important contributions, both deviatoric and isotropic, to the stress field in the interior of the TPE inclusion.

Previous considerations refer to a disc of infinitesimal thickness. A disc of finite thickness can be modelled expressing in cylindrical coordinates the solutions for displacement and strain of Section 5.3 and 5.4, respectively, assuming that: (i) the aspect ratio of the disc is low, that is $b/a_0 \ll 1$ and (ii) the δ-function appearing in the ϵ_{zz} component inside the disc is approximated as in eq. (67). In this way we see that for $\rho < a_0$ and $|z| < b/2$, the component $\tau_{\rho z}$ vanishes only in $z = 0$ but generally it is not equal to zero within the disc. Moreover, in order to represent a non uniform TPE potency inside a disc it is possible to consider piled up thin discs, as shown in the following section.

7 THE EFFECTS OF A TPE DISC ON SEISMICITY

Inside the TPE disc, we can see from eq. (68) that $\epsilon_{\varphi\varphi}$ is always less than $\epsilon_{\rho\rho}$ and, since $b \ll a_0$ (by assumption), we have generally $\tau_{zz}^{(D)} \gg \tau_{\rho\rho}^{(D)} > \tau_{\varphi\varphi}^{(D)}$ promoting thrust faulting, if z is assumed vertical (apart from the region $\rho \simeq a_0$ where the series may attain large values and the order of principal stresses is reversed). The opposite holds in the elastic region above the disc, where $\tau_{zz}^{(el)} < \tau_{\rho\rho}^{(el)} < \tau_{\varphi\varphi}^{(el)}$ suggesting a normal faulting environment if z is vertical (apart from the region $\rho \simeq a_0$). In any case, the deviatoric stress inside the TPE disc is much higher than outside (Fig. 9).

The maximum shear traction within the TPE disc acts on 45° dipping, radially striking surfaces, within most of the TPE region. However, given the compressive environment and the small difference between $\tau_{\rho\rho}^{(D)}$ and $\tau_{\varphi\varphi}^{(D)}$, even a moderate component of pre-stress may alter the order of these principal stresses, favouring reverse ring faulting when $\tau_{\varphi\varphi}$ is the intermediate stress.

To better understand the effect of a TPE source on seismicity, it is worth introducing the induced change of Coulomb failure function (ΔCFF, e.g. Wang 2017; Nespoli *et al.* 2018) generated by the TPE inclusion which can be computed according to

$$\Delta\mathrm{CFF} = |\tau| + f(\sigma_n + p), \tag{72}$$

where τ and σ_n are the shear and the normal traction change induced by the TPE inclusion on a fault plane, respectively, p is the pore pressure change and f is the friction coefficient. Specifically, we compute the ΔCFF induced by different TPE potency distributions within two or more discs of finite thickness. In so doing we account for a smaller TPE potency in the upper part of the disc (green region in Fig. 1), with respect to the lower one, owing to a vanishing temperature change. As reported in Section 4, this configuration is suitable to model, at a given time, a sharp temperature front propagating across both discs, with advective mechanism driven by a uniform pressure gradient.

Table 1. Values of thermo-poro-elastic parameter pertinent to highly porous sedimentary rocks (Rice & Cleary 1976), as assumed in the present work.

Thermo-poro-elastic parameters		
Rigidity	μ	6 GPa
Poisson's ratio	ν	0.2
Poroelastic constant	H	10 GPa
Thermal expansion (solid)	α_s	$3 \times 10^{-5}\ K^{-1}$

Table 2. Pore pressure p and temperature T changes assumed in three different cases of TPE inclusion with finite thickness, constituted by two depth ranges (n.1 = deep, $-100\ \text{m} \le z < 0$; n.2 = shallow, $0 \le z < 100$ m). For both depth ranges it is reported whether the internal stress field is extensional (favouring normal faults) or compressive (favouring thrust faults). Cases 2 and 3 are obtained overlapping two TPE discs.

		Finite thickness TPE inclusion		
		Case 1	Case 2	Case 3
$-100\ \text{m} \le z < 0$	T_1 [K]	100	100	97
	p_1 [MPa]	1	1	10
	ϵ_{01}	1×10^{-3}	1×10^{-3}	1×10^{-3}
	Environment	Compressive	Compressive	Compressive
$0 \le z < 100$ m	T_2 [K]	100	0	97
	p_2 [MPa]	1	0.5	10
	ϵ_{02}	1×10^{-3}	2×10^{-5}	1×10^{-3}
	Environment	Compressive	Extensional	Compressive

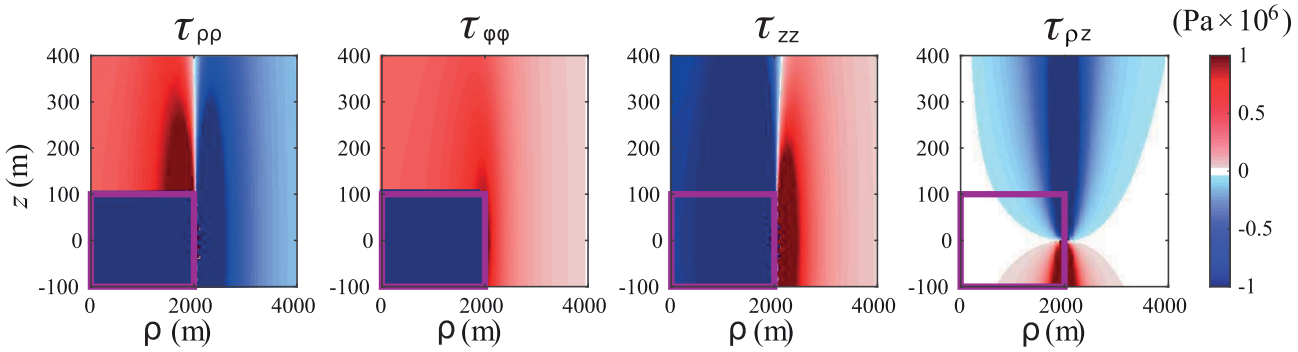

Figure 10. Stress field generated by a 200-m-thick TPE disc with radius $a_0 = 2000$ m, with a uniform TPE inclusion potency $\epsilon_0 = 1 \times 10^{-3}$ (e.g. $T = 100$ K and $p = 1$ MPa or $T = 97$ K and $p = 10$ MPa), assuming the thermo-poro-elastic parameters reported in Table 1. Plot are obtained using series truncation at $N = 1000$.

7.1 Finite thickness disc

First, we study the case of a TPE disc with finite thickness (Case 1 in Table 2) with a homogeneous TPE inclusion potency inside. Stress components using parameter values (Table 1) pertinent to highly porous sedimentary rocks (e.g. Rice & Cleary 1976; Wang 2017) are shown in Fig. 10.

It is worth noting that, even in the case of a finite thickness disc, the 'welded boundary conditions' over the top and bottom disc faces (which require the continuity of tractions $\tau_{\rho z}$, τ_{zz}) are fulfilled. Differently from a TPE source with infinitesimal thickness, for which $\tau_{\rho z} = 0$ inside the inclusion (see Section 6), in the case of a finite-thickness disc a small shear component $\tau_{\rho z}$ appears close to the lateral boundaries of the inclusion, even in its interior (Fig. 10).

Thanks to the translational invariance $G_{ij}(\mathbf{x}, \mathbf{x}') = G_{ij}(\mathbf{x} - \mathbf{x}')$ of the Green's function in an unbounded elastic medium, the solution S for the stress field produced by two vertically piled-up, finite-thickness discs, D_1 and D_2, with thickness b_1 and b_2 and TPE potency ϵ_{01} and ϵ_{02}, respectively, may be easily obtained adding the solution S_1 for D_1 alone to the solution S_2 for D_2 alone, which is vertically shifted of b_1 with respect to S_1. In particular, within the lower disc the solution, S is obtained as the sum of the internal solution, $S_1^{(S)}$ and the external solution, $S_2^{(el)}$. Within the upper disc, S is the sum of $S_1^{(el)}$ and $S_2^{(S)}$. Above the upper disc (and below the lower disc), S is given by the sum of $S_1^{(el)}$ and $S_2^{(el)}$. The representation of piled-up discs may be generalized in an obvious way to approximate a disc with finite thickness b through its decomposition in n thin discs, each with intensity ϵ_{0k} and thickness $b_k = \frac{b}{n}$, $k = 1, 2, \ldots n$, emplaced between $z = -\frac{b}{2}$ and $z = \frac{b}{2}$. It is worth to note that the solution of a thin disc with a finite thickness $b \ll a_0$ and a uniform TPE inclusion potency ϵ_0 (Fig. 10) can be obtained as reported at the end of Section 6 or equivalently, with two (or more) piled-up discs with $\epsilon_{0k} = \epsilon_0$.

Fig. 11 shows the stress field generated by a TPE inclusion in which the lower disc (from $z = -100$ m to $z = 0$) is affected by T_1 and p_1, while the upper disc (from $z = 0$ to $z = 100$ m) is affected by $T_2 = 0$ and $p_2 = \frac{1}{2} p_1$ (Case 2 in Table 2). Such a configuration is suitable to

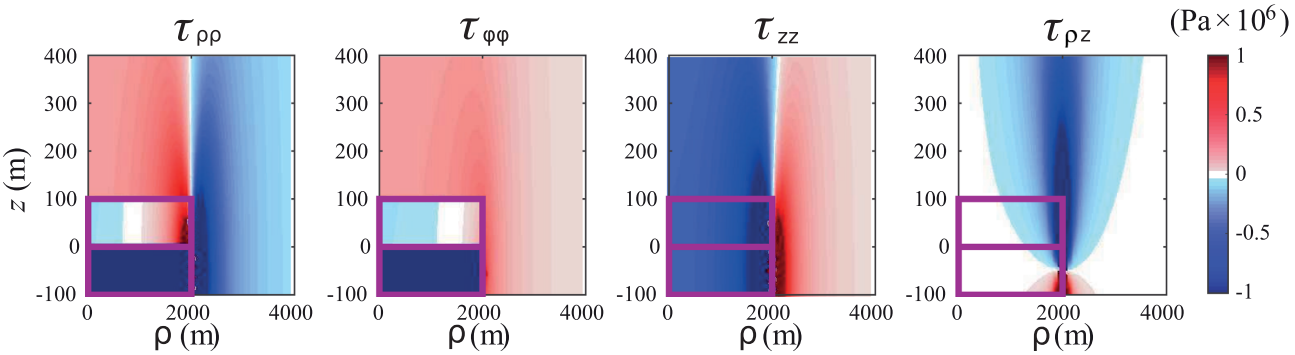

Figure 11. (a) Stress field generated by a 200-m-thick TPE disc with radius $a_0 = 2000$ m composed by a lower disc (-100 m $\leq z < 0$) with a TPE inclusion potency $\epsilon_{01} = 1 \times 10^{-3}$ (e.g. $T_1 = 100$ K and $p_1 = 1$ MPa) and an upper disc ($0 \leq z < 100$ m) with $\epsilon_{02} = 2 \times 10^{-5}$ (e.g. $T_2 = 0$ K and $p_2 = 0.5$ MPa), assuming the thermo-poro-elastic parameters reported in Table 1. Plot are obtained using series truncation at $N = 1000$.

model a TPE inclusion when the thermal front of the fluids has reached only half thickness of the inclusion (Fig. 2b.) The low TPE inclusion potency of the upper disc leads to a lower stress magnitude with respect to the case with uniform TPE potency (Fig. 10). Furthermore, $\tau_{\rho\rho}$ changes sign (from $\tau_{\rho\rho} < 0$ to $\tau_{\rho\rho} > 0$) laterally within the upper disc (compare Figs 10 and 11). This effect is due to the 'interaction' between the two discs: the stronger and deeper disc induces within the weaker upper disc an extensional contribution to $\tau_{\rho\rho}$, $S_1^{(el)}$. There, the compressive contribution generated by the upper disc onto itself, $S_2^{(S)}$, is smaller in magnitude than $S_1^{(el)}$. Only in Case 2 we obtain an extensional environment, favouring normal faults, within the TPE inclusion (Table 2), where generally a compressive environment, favouring thrust faults, is present, in agreement with results obtained for a disc of infinitesimal thickness (Fig. 9).

The ΔCFF is computed assuming optimally oriented fault planes (the ones where ΔCFF is maximum) for the two cases (Table 2) shown in Figs 10 and 11. The resulting ΔCFF are computed in vertical sections (Figs 12a–i) and in a vertical profile along the disc axis ($\rho = 0$) for three different values of friction ($f = 0.2$, 0.4 and 0.8). In all cases the ΔCFF is discontinuous at the top of the TPE disc. In Case 2 a second discontinuity arises at the interface between the two TPE discs. The discontinuities are due to the strong difference between the magnitude of deviatoric stress inside and outside a disc, as evidenced at the beginning of this Section (Fig. 9). In Case 1, with uniform ϵ_0, regardless of the friction coefficient, inside the inclusion the ΔCFF reaches the highest value on the axis of symmetry of the disc and it gradually decreases towards the lateral boundaries (Fig. 12). This result is due to the strong reduction of the deviatoric-stress component magnitude near the lateral boundaries of the TPE disc (Fig. 9). The ΔCFF is positive in almost all the vertical sections, apart from Case 1 with $f = 0.4$ and 0.8 (Figs 12b and c), where ΔCFF assumes slightly negative values near the lateral boundaries of the inclusion. A similar behaviour was also envisaged by Belardinelli *et al.* (2019) who found that high T/p ratios, in conjunction with high friction coefficients, can lead to negative ΔCFF values close to the external boundary of a spherical-shell shaped TPE inclusion.

Along the axis of symmetry of the inclusion ($\rho = 0$, –100 m $< z <$100 m), in the case of uniform T and p (Case 1), the magnitude of ΔCFF decreases for higher friction coefficients. Differently, in the case of lower T and p in the upper disc (Case 2), this trivial effect is observed only in the lower disc. In Case 2, the increase of ΔCFF in the upper disc, by increasing friction, is due to the extensional stress field induced by the deeper disc (by means of $S_1^{(el)}$), which prevails over the compressive stress caused by $S_2^{(S)}$ inside the shallower disc, as already explained.

In Case 3 the TPE inclusion potency is uniform, with the same value as in Case 1, but it was obtained from eq. (2), assuming a greater pore-pressure and a lower temperature, uniformly distributed within the TPE inclusion ($p_1 = p_2 = 10$ MPa and $T_1 = T_2 = 97$ K). As in Case 1, the maximum ΔCFF, for each z, is obtained within the disc, along its symmetry axis. Even if the stress field generated in both cases is the same (Fig. 10), inside the TPE source the induced ΔCFF is greater in Case 3 with respect to Case 1 (Fig. 12), because in Case 3 the higher pore pressure strongly reduces the frictional resistance (*lubrication effect*). This is confirmed by the effect of the friction coefficient shown in Fig. 12: in Case 3 the ΔCFF increases for larger friction coefficients, unlike Case 1. Results of Fig. 12 confirm that optimally oriented dip-slip faults are distributed around and within the TPE disc, with the same mechanisms as deemed considering the order of stress components shown in Figs 10 and 11.

7.2 Seismicity due to fluid extraction

Even if the previous paragraphs were focused on volcanological applications, in which hot and pressurized fluids are injected into the TPE inclusion, the solutions provided in the present paper are also suitable to model fluid withdrawal in geothermal fields. Fig. 13 shows an example of application of a TPE inclusion, suitable to model fluid production from a deep reservoir, as modelled by Segall & Fitzgerald (1998) assuming an isothermal reduction in pore pressure. It was obtained assuming a negative TPE inclusion potency, ϵ_0, that arises from $p < 0$ and $T = 0$. Fig. 13 a shows the expected fault mechanisms due to fluid withdrawal, as commonly reported in geothermal environments (Segall 1989; Bardainne *et al.* 2008; Chang & Segall 2016; Wang & Manga 2021): normal faulting can be promoted within and near the periphery of the reservoir, while reverse faulting can be favoured above and below the reservoir. As we can see from Fig. 13b, this heterogeneity of

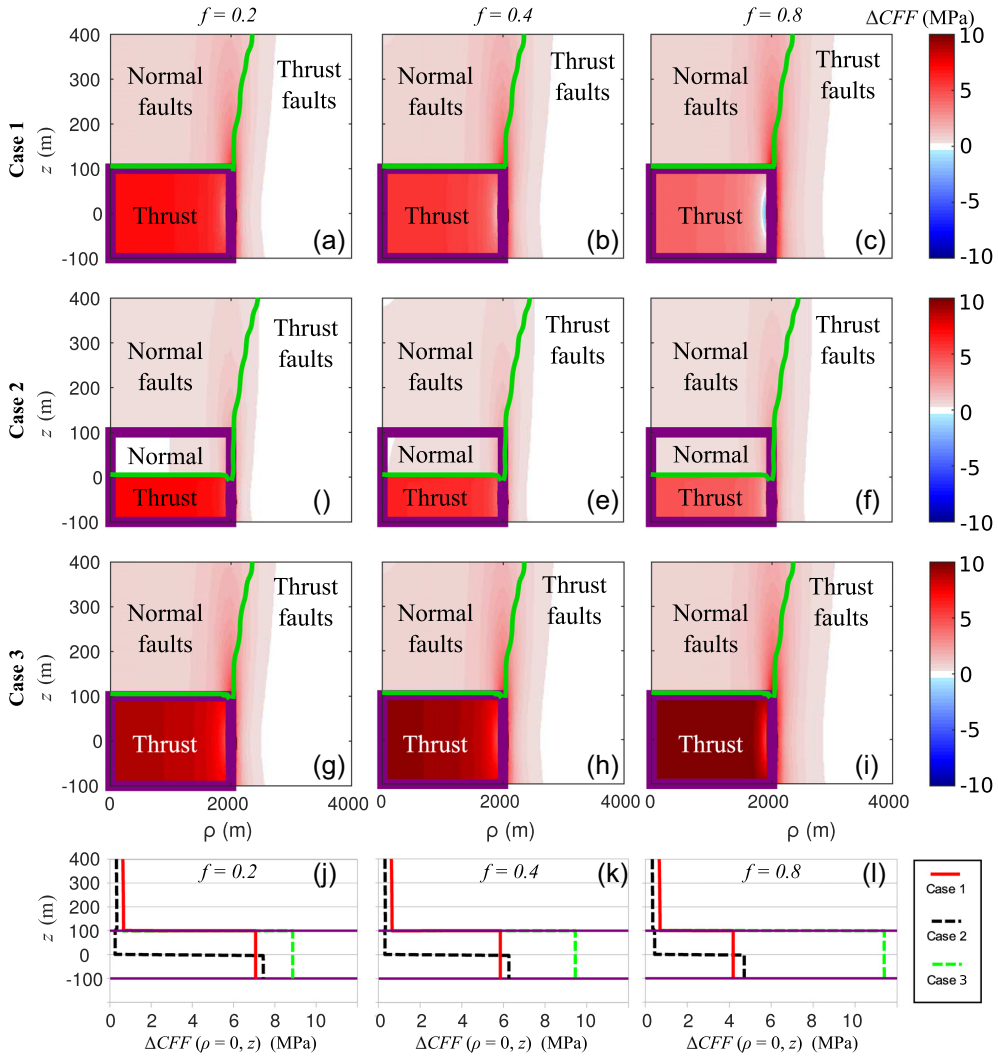

Figure 12. ΔCFF (colour) generated on optimally oriented fault planes by a 200-m-thick TPE disc with radius $a_0 = 2000$ m, for Case 1 (a–c), Case 2 (d–f), Case 3 (g–i), reported in Table 2 and for three different friction coefficients $f = 0.2$ (a, d, g), 0.4 (b, e, h), 0.8 (c, f, i). Green lines separate zones where normal faulting is favoured, from the ones of thrust faulting. Bottom panels (j, k, l) show ΔCFF profiles computed along the axis of symmetry of the inclusions ($\rho = 0, z$). Purple boxes and lines indicate the location of the boundary of the TPE inclusions.

fault mechanisms inside and in the surrounding of the reservoir, is reproduced with our solutions for a TPE inclusion with negative potency. A negative potency is also obtained in a geothermal reservoir where re-injection of cold ($T < 0$) fluids is used to maintain constant pressure ($p = 0$) after its exploitation. In the case of fluid injection with $p > 0$ and $T > 0$ (Fig. 12), the distribution of optimally oriented faults had opposite mechanisms with respect to the case of fluid withdrawal (Fig. 13). In particular, thrust faults were favoured within the inclusion.

8 DISCUSSION

In this paper we provide analytical solutions for displacement, strain and stress field for a disc shaped TPE inclusion embedded in a homogeneous full-space. The series expansions appearing in our solutions provide fast convergence in all the full-space, apart from $r = a_0$, where the series diverge. The infinite singularity of u_r (and e_{rr}) along the disc rim is clearly unphysical since u_r should be continuous in $r = a_0$ and, even more important, this singularity would entail interpenetration of matter. A similar problem arises in the framework of tensile dislocations with assigned Burgers vectors (Landau & Lifshits 1967). In analogy with the mentioned dislocation problem, the unphysical singularity may be removed assuming that temperature and pore pressure changes T and p vanish gradually when $\rho \to a_0$: this would make u_ρ bounded along the disc rim.

Of course, the models presented above are applicable to *deep* TPE sources, that is having depths greater than the lateral extent, since the effects due to the proximity of the free surface cannot be obtained using the present method based on a displacement potential, because the Green's function in a half-space is no longer symmetric and eqs (10)–(12) no longer hold. Nevertheless, for a horizontal TPE disc in a half-space bounded by a free surface, Mantiloni *et al.* (2020) showed that semi-analytic solutions can be obtained separating Mindlin's Green's function (Mindlin 1936) into a singular component, the explicit expressions of which are provided in the present paper, and a regular

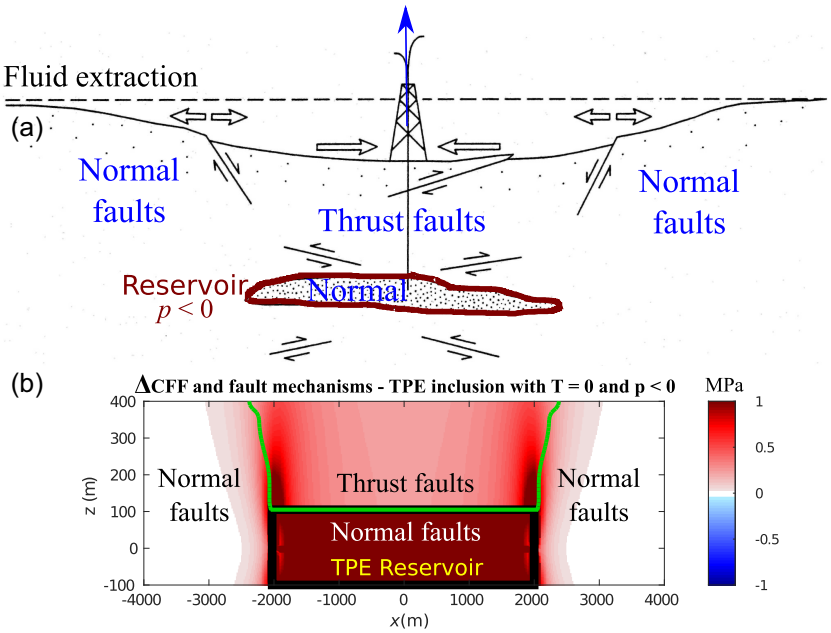

Figure 13. Example showing how to model mechanical effects on seismicity due to geothermal production (fluid extraction) in a TPE reservoir. (a) Sketch of observed faulting mechanisms due to fluid withdrawal from a geothermal reservoir (modified after Segall 1989). (b) ΔCFF (colour) and expected fault mechanisms due to a TPE inclusion assuming $p = -10$ MPa and $T = 0$ ($\epsilon_0 = -3 \times 10^{-4}$), $f = 0.2$ and the thermo-poro-elastic parameters reported in Table 1. Green lines separate zones where normal faulting is favoured, from the ones of thrust faulting, as also reported. The black box indicates the location of the boundary of the TPE inclusion.

component coping with the free surface conditions which was evaluated numerically. For a deep source and in near-field condition, where the induced seismicity is expected to occur (e.g. Nespoli *et al.* 2021), the regular components can be neglected and the stress field estimated through eq. (71) well approximates the total stress even in the presence of a free surface. Differently from Mantiloni *et al.* (2020), in the present model the external stress field is entirely deviatoric, as due to the absence of the free surface condition and this allows writing $\epsilon_{kk} = \epsilon_1$, leading to a simpler pressure diffusion equation. As in Belardinelli *et al.* (2019), in the far field, displacements and stresses are asymptotically equal (within a multiplicative factor) to those provided by a pressurized spherical cavity.

The displacement of a TPE disc scales with Aa_0, while stress scales with $2\mu\epsilon_1$ (see sections 5.3 and 6). It is worth noting that this is still true for discs of very large thickness ($b \approx a_0$), since they can be represented by superimposition of several TPE discs with small ($b \ll a_0$) thickness, following the procedure outlined in Section 6.1. We recall that both A and ϵ_1 are proportional to the TPE inclusion potency ϵ_0 (eqs 11 and 37, respectively). Then according to our model, in order to evaluate the numerical amplitude of TPE effects expected in a volcanic (or, more generally, geothermal) environment, it is necessary to estimate reasonable values of the TPE inclusion potency ϵ_0, which in turn linearly depends on p and T (eq. 2). Using parameter values pertinent to highly porous sedimentary rocks (Table 1), as in Section 6, and reasonable estimates of T and p (see Section 4.1), a temperature increase $T = 100$ K without any pore pressure increase (i.e. $p = 0$, $\epsilon_0 = 0.001$) within a disc with $a_0 = 1$ km and $b = \frac{1}{10}a_0 = 100$ m provides the following numerical values of the normalization constants: $2\mu\epsilon_1 = 18 \times 10^6$ Pa for stress components, $Aa_0 = 7.5$ cm for the displacement; if a pore pressure increase $p = 10$ MPa applies without any temperature increase (i.e. $T = 0$, $\epsilon_0 = 3.3 \times 10^{-4}$) the following values are obtained for the normalization constants: $2\mu\epsilon_1 = 0.6 \times 10^6$ Pa for stress components, $Aa_0 = 0.25$ cm for the displacement. Even if the temperature effects seem much more relevant than the pore pressure effects, it must be mentioned that the geometrical extension of temperature changes is expected to increase much more slowly than pore pressure changes, in a high permeability medium, since the propagating fluid rapidly cools down while crossing the colder rock matrix (Nespoli *et al.* 2021).

Furthermore, even if the pore pressure provides smaller effects than T (for most rocks), the importance of p in promoting faulting processes within the TPE region is enhanced by its lubrication effects, according to the modified Mohr–Coulomb criterion (Section 7.1). In fact, under the same TPE inclusion potency ϵ_0, effects on induced seismicity are larger for greater p and lower T (Case 3 in Fig. 12 to be compared with Case 1).

Assuming a uniform TPE inclusion potency as in the case of the thin disc or Cases 1 and 3, we can provide an estimate of pore pressure changes suitable to realize positive ΔCFF for an assigned T value according to the following consideration. As tensile stresses are assumed positive, the friction resistance decreases both if the normal stress within the solid matrix, σ_n, increases ($\sigma_n > 0$) or if the pore pressure, p, increases. Actually, within the TPE inclusion an increase of confining pressure $-\frac{1}{3}\tau_{kk}^{(S)} = \frac{4}{3}\mu\epsilon_1$ (eq. 70) occurs, so that a decrease of normal stress is expected ($\sigma_n < 0$). Roughly assuming that $\sigma_n \sim \frac{1}{3}\tau_{kk}^{(S)}$, in order to reduce friction the pore pressure increase should exceed the

confining pressure increase. To this aim, friction is reduced if $p > -\frac{1}{3}\tau_{kk} = \frac{4}{3}\mu\epsilon_1 = cT$ with

$$c = \frac{\mu\alpha_s}{\left[\frac{9}{4}\frac{1-\nu}{1+\nu} - \frac{\mu}{H}\right]} = 2 \times 10^5 \text{ Pa K}^{-1}, \tag{73}$$

where the estimate is made using the values of TPE parameters μ, ν, H, α_s reported in Table 1. For a given temperature change T, $p = cT$ is an upper estimate of the pore pressure change suitable to counterbalance the change in normal stress due to the intrusion of hot and pressurized fluids within the TPE inclusion. This can be explained considering that the increase of confining pressure overestimates the increase of compressive normal stress, $-\sigma_n$, on optimally oriented planes. The lubrication effect is negligible in our Case 1 because $p \ll cT$, unlike Case 3 where $p \simeq cT$ (Fig. 12).

9 CONCLUSIONS

The TPE disc model shows that a significant deviatoric stress is generated by changes of pore pressure p and temperature T within it. If the ground surface is assumed to lay above the TPE disc, this is if z is vertical, for positive increments of p and T, the induced stress field and the expected heterogeneity of focal mechanisms can be summarized as follows:

(i) The compressive stress axis within the disc is horizontal, so that thrust faulting mechanisms are favoured within the TPE disc over optimally oriented faults.
(ii) Above the inclusion, in the elastic domain the compression axis is vertical, favouring normal faulting mechanisms as also obtained by the spherical shell model of Belardinelli *et al.* (2019) and the model of Mantiloni *et al.* (2020).
(iii) Even in the interior of the TPE inclusion, an extensional environment, that is normal faulting mechanisms, can be obtained assuming a temperature gradient much steeper than the pressure gradient, as we expect during the vertical uprise of hot and pressurized fluids.

Inverse faulting mechanism confined in a bounded region can suggest the presence of a TPE source with $\epsilon_0 > 0$ located in the same region. Looking at Figs 9, 10 and 11 we may speculate that radially striking faults should be favoured with respect to ring faults (since $\tau_{\rho\rho}$ is the intermediate principal stress), but the role of the initial stress (before p and T were imposed) is crucial in determining the order of principal stresses between $\tau_{\rho\rho}$ and $\tau_{\varphi\varphi}$. If a nearly uniform component of regional tectonic stress is dominant, the strike direction is the radial direction parallel to the compressive tectonic axis; if a local axially symmetric field was originally present, with compressive axis in the radial direction, ring faults are to be expected within the TPE region.

TPE models are suitable to describe hot fluids ascending from a deep reservoir, causing temperature and pore pressure increases in the overlying region. Our results show that at least in the central part of the TPE disc basis surface shear tractions vanish. Thus the solution applies even if the TPE disc overlays a fluid magma reservoir, because the usual boundary conditions imposed at a solid/fluid interface are fulfilled. The present model is also suitable for applications in geothermal contexts to represent fluid re-injection or production, assuming $T < 0$ and $p = 0$ or $T = 0$ and $p < 0$, respectively (Segall & Fitzgerald 1998).

If crustal elastic heterogeneities or an arbitrary TPE inclusion shape are to be taken into account, numerical models should be used (e.g. Nespoli *et al.* 2021). The present solution allows us to test numerical models in near field for a TPE disc located in a homogeneous medium. The proposed model may be easily generalized to account for p and T variable with z and ρ within the TPE disc since, realistically, they both should vanish gradually when approaching the elastic domain. Such a generalization most probably allows preventing the singularity of the solution at the disc lateral surface too and is left for future developments.

ACKNOWLEDGMENTS

The authors would like to thank the editors and the anonymous reviewers for their constructive comments. The authors also thank Irene Lamberti for her contributions to the study of series convergence.

DATA AVAILABILITY

The code relating to this work is available from https://github.com/Massimones/TPE-disk.git.

REFERENCES

Abramowitz, M. & Stegun, I., 1965. *Handbook of Mathematical Functions: With Formulas, Graphs, and Mathematical Tables, Applied mathematics series,* Dover Publications.

Aki, K. & Richards, P.G., 2002. *Quantitative Seismology,* 2nd edn, University Science Books.

Bardainne, T., Dubos-Salle, N., Snchal, G., Gaillot, P. & Perroud, H., 2008. Analysis of the induced seismicity of the Lacq Gas Field (southwestern France) and model of deformation, *Geophys. J. Int.,* **172**(3), 1151–1162.

Bejan, A., 1984. *Convection Heat Transfer,* Wiley.

Belardinelli, M., Bizzarri, A., Berrino, G. & Ricciardi, G., 2011. A model for seismicity rates observed during the 1982–1984 unrest at Campi Flegrei Caldera (Italy), *Earth planet. Sci. Lett.,* **302**(3), 287–298.

Belardinelli, M., Bonafede, M. & Nespoli, M., 2019. Stress heterogeneities and failure mechanisms induced by temperature and pore-pressure increase in volcanic regions, *Earth planet. Sci. Lett.,* **525,** doi:10.1016/j.epsl.2019.115765.

Bianco, F., Del Pezzo, E., Saccorotti, G. & Ventura, G., 2004. The role of hydrothermal fluids in triggering the July-August 2000 seismic swarm

at Campi Flegrei, Italy: evidence from seismological and mesostructural data, *J. Volc. Geotherm. Res.,* **133**(1), 229–246.

Biot, M.A., 1941. General theory of three-dimensional consolidation, *J. Appl. Phys.,* **12**(2), 155–164.

Bonafede, M. & Mazzanti, M., 1997. Hot fluid migration in compressible saturated porous media, *Geophys. J. Int.,* **128**(2), 383–398.

Calò, M. & Tramelli, A., 2018. Anatomy of the Campi Flegrei Caldera using enhanced seismic tomography models, *Sci. Rep.,* **8**(16254) , doi:10.1038/s41598-018-34456-x.

Chang, K. & Segall, P., 2016. Seismicity on basement faults induced by simultaneous fluid injection-extraction, *Pure appl. Geophys,* **173,** 2621–2636.

D'Auria, L., Massa, B., Cristiano, E., Gaudio, C.D., Giudicepietro, F., Ricciardi, G. & Ricco, C., 2014. Retrieving the stress field within the Campi Flegrei Caldera (Southern Italy) through an integrated geodetical and seismological approach, *Pure appl. Geophys.,* **172**(11), 3247–3263.

Eshelby, J.D., 1957. The determination of the elastic field of an ellipsoidal inclusion, and related problems, *Proc. R. Soc. Lond., A,* **241**(1226), 376–396.

Fjær, E., Holt, R., Horsrud, P. & Raaen, A., 2008. *Petroleum Related Rock Mechanics,* Elsevier Science.

Fung, Y., 1965. *Foundations of Solid Mechanics,* Prentice-Hall International Series in Dynamics, Kluwer Academic Publishers.

Geertsma, J., 1973. Land subsidence above compacting oil and gas reservoirs, *J. Petrol. Techol.,* **25**(06), 734–744.

Gischig, V., Wiemer, S. & Alcolea, A., 2014. Balancing reservoir creation and seismic hazard in enhanced geothermal systems, *Geophys. J. Int.,* **198**(3), 1585–1598.

Guido, F.L., Antonellini, M. & Picotti, V., 2015. Modeling ground displacement above reservoirs undergoing fluid withdrawal/injection based on an ellipsoidal inhomogeneity model, *Int. J. Rock. Mech. Min. Sci.,* **79,** 63–69.

Heap, M.J. *et al.*, 2021. The tensile strength of volcanic rocks: experiments and models, *J. Volc. Geotherm. Res.,* **418,** doi:10.1016/j.jvolgeores.2021.107348.

Jackson, J.D., 1999. *Classical Electrodynamics,* John Wiley and Sons.

Landau, L. & Lifshits, E., 1967. *Physique théorique: Théorie de l'élasticité,* Vol. **7,** Mir.

Lima, A., PBodnar, R.J., De Vivo, B., Spera, F. & Belkin, H., 2021. Interpretation of recent unrest events (Bradyseism)at Campi Flegrei, Napoli (Italy): comparison of models based on cyclical hydrothermal events versus shallow magmatic intrusive events, *Geofluids,* **2021**(2000255), 1–16.

Lund, B., Lindman, M., Arvidsson, M., Slunga, R. & Bödvarsson, R., 2005. Stress variations before and during the two M=6.5 earthquakes of June 2000 in the South Iceland Seismic Zone., in *AGU Fall Meeting Abstracts,* Vol. **2005,** pp. T21B–0468.

Mantiloni, L., Nespoli, M., Belardinelli, M.E. & Bonafede, M., 2020. Deformation and stress in hydrothermal regions: the case of a disk-shaped inclusion in a half-space, *J. Volc. Geotherm. Res.,* **403,** 107011 , doi:10.1016/j.jvolgeores.2020.107011.

McTigue, D.F., 1986. Thermoelastic response of fluid-saturated porous rock, *J. geophys. Res.,* **91**(B9), 9533–9542.

Minakov, A. & Yarushina, V., 2021. Elastoplastic source model for microseismicity and acoustic emission, *Geophys. J. Int.,* **227**(1), 33–53.

Mindlin, R.D., 1936. Force at a point in the interior of a semi-infinite solid, *Physics,* **7**(5), 195–202.

Nespoli, M., Belardinelli, M., Gualandi, A., Serpelloni, E. & Bonafede, M., 2018. Poroelasticity and fluid flow modeling for the 2012 Emilia-Romagna Earthquakes: hints from GPS and InSAR data, *Geofluids,* **2018** , doi:10.1155/2018/4160570.

Nespoli, M., Belardinelli, M.E. & Bonafede, M., 2021. Stress and deformation induced in layered media by cylindrical thermo-poro-elastic sources: an application to Campi Flegrei (Italy), *J. Volc. Geotherm. Res.,* **415,** 107269 , doi:10.1016/j.jvolgeores.2021.107269.

Pu, H.-C., Lin, C.-H., Lee, H.-F., Lai, Y.-C., Chang, L.-C. & Shih, M.-H., 2021. Ascending volcanic fluids portended by spatiotemporal variations of the earthquake mechanisms in the Tatun Volcano Group in northern Taiwan, *Geophys. Res. Lett.,* **48**(9), e2020GL091686 , doi:10.1029/2020GL091686.

Rice, J.R. & Cleary, M.P., 1976. Some basic stress diffusion solutions for fluid-saturated elastic porous media with compressible constituents, *Rev. Geophys.,* **14**(2), 227–241.

Rinaldi, A.P. & Nespoli, M., 2017. Tough2-seed: a coupled fluid flow and mechanical-stochastic approach to model injection-induced seismicity, *Comp. Geosci.,* **108,** 86–97.

Rudnicki, J., 1999. Alteration of regional stress by reservoirs and other inhomogeneities: stabilizing or destabilizing?, in *Paper Presented at the 9th ISRM Congress,* Paris, France, 25–28 August 1999, Paper Number: ISRM-9CONGRESS-1999-303.

Saccorotti, G., Bianco, F., Castellano, M. & Del Pezzo, E., 2001. The July-August 2000 seismic swarms at Campi Flegrei Volcanic Complex, Italy, *Geophys. Res. Lett.,* **28**(13), 2525–2528.

Schlindwein, V., Demuth, A., Geissler, W.H. & Jokat, W., 2013. Seismic gap beneath Logachev seamount: indicator for melt focusing at an ultraslow mid-ocean ridge?, *Geophys. Res. Lett.,* **40**(9), 1703–1707.

Schuler, J., Pugh, D.J., Hauksson, E., White, R.S., Stock, J.M. & Brandsdttir, B., 2016. Focal mechanisms and size distribution of earthquakes beneath the Krafla central volcano, NE Iceland, *J. geophys. Res.,* **121**(7), 5152–5168.

Segall, P., 1989. Earthquakes triggered by fluid extraction, *Geology,* **17**(10), 942–946 , doi:10.1130/0091-7613(1989)017<0942:ETBFE>2.3.CO;2.

Segall, P., 1992. Induced stresses due to fluid extraction from axisymmetric reservoirs, *Pure appl. Geophys.,* **139**(3), 535–560.

Segall, P. & Fitzgerald, S.D., 1998. A note on induced stress changes in hydrocarbon and geothermal reservoirs, *Tectonophysics,* **289**(1), 117–128.

Shapiro, S.A., 2015. *Fundamentals of Poroelasticity,* pp. 48–117, Cambridge Univ. Press.

Sigurdsson, H., Houghton, B., Rymer, H., Stix, J. & McNutt, S., 1999. *Encyclopedia of Volcanoes,* Elsevier Science.

Skempton, A.W., 1954. The pore-pressure coefficients a and b, *Géotechnique,* **4**(4), 143–147.

Stefansson, R., Bonafede, M. & Gudmundsson, G.B., 2011. Earthquake-prediction research and the earthquakes of 2000 in the South Iceland Seismic Zone, *Bull. seism. Soc. Am.,* **101**(4), 1590–1617.

Todesco, M., 2021. Caldera's breathing: poroelastic ground deformation at Campi Flegrei (Italy), *Front. Earth Sci.,* **9,** 691 , doi:10.3389/feart.2021.702665.

Trasatti, E., Bonafede, M., Ferrari, C., Giunchi, C. & Berrino, G., 2011. On deformation sources in volcanic areas: modeling the Campi Flegrei (Italy) 1982–84 unrest, *Earth planet. Sci. Lett.,* **306**(3–4), 175–185.

Turcotte, D. & Schubert, G., 2014. *Geodynamics,* Cambridge Univ. Press.

Villumsen, J.V., 1983. The vertical growth and structure of galactic disks, *Astrophys. J.,* **274,** 632–645.

Villumsen, J.V., 1985. Evolution of the velocity distribution in galactic disks, *Astrophys. J.,* **290,** 75–85.

Wang, C.-Y. & Manga, M., 2021. Earthquakes influenced by water, *Lecture Not. Earth Sci.,* **114,** 125–139.

Wang, H.F., 2017. *Theory of Linear Poroelasticity with Applications to Geomechanics and Hydrogeology,* Princeton Univ. Press.

Wangen, M. & Halvorsen, G., 2020. A three-dimensional analytical solution for reservoir expansion, surface uplift and caprock stress due to pressurized reservoirs, *Math. Geosci.,* **52**(2), 253–284.

Zencher, F., Bonafede, M. & Stefansson, R., 2006. Near-lithostatic pore pressure at seismogenic depths: a thermoporoelastic model, *Geophys. J. Int.,* **166**(3), 1318–1334.

APPENDIX: NOTES ON CONVERGENCE OF SERIES IN SECTIONS 5.3 AND 5.4

Absolute convergence of the series for the displacement components u_r and u_θ is proved if $r \neq a_0$ (e.g. using D'Alambert's criterion). When $r \to \infty$, u_r (eq. 39) decreases asymptotically as $\sim r^{-2}$ and u_θ (eq. 41) as $\sim r^{-4}$. In the following of the Appendix we focus on the cases $r \leq a_0$. When $r = a_0$ and $\theta \neq \frac{\pi}{2}$ convergence for u_r is extremely slow while u_θ diverges. For both components analytic continuation may be preferably used to estimate their values in $r \simeq a_0$. In $r = a_0$ and $\theta = \frac{\pi}{2}$ a logarithmic singularity is present in u_r while u_θ vanishes. It is worth to recall that u_θ is an odd function of $x = \cos\theta$: it vanishes continuously in $\theta = \frac{\pi}{2}$ if $r > a_0$ but a jump discontinuity from $-Aa_0$ to $+Aa_0$ is present when $\theta = \frac{\pi}{2}^{\mp}$ if $r < a_0$.The resulting trends of u_r and u_θ are shown in Figs 4 and 5.

A1 Radial component of displacement (eq. 49)

The series appearing in eq. (49) is absolutely convergent if $r/a_0 < 1$ since $\left|c_{2m} P_{2m}(x) \frac{2m}{2m-1}\right| \leq 1$ and, using the sum of the geometric series, we get

$$\sum_{m=1}^{\infty} \left| c_{2m} P_{2m}(x) \frac{2m}{2m-1} \left(\frac{r}{a_0}\right)^{2m-1} \right| \leq \frac{1}{\sqrt{t}} \sum_{m=1}^{\infty} t^m = \frac{\sqrt{t}}{1-t},$$

where $t = \left(\frac{r}{a_0}\right)^2 < 1$ and we have taken into account the asymptotic trend (eq. 30) and the property $|P_n(x)| \leq 1, \ \forall n$. The number N of terms needed to get a fair approximation of the series in eq. (49) is strongly dependent on the value r/a_0: we may evaluate N according to the following scheme. The rest R_N of the series of absolute values is such that

$$R_N \leq \sum_{m=N+1}^{\infty} t^{m-1/2} = \frac{t^{N+1/2}}{1-t} < \frac{t^N}{1-t}.$$

Then R_N is negligible (i.e. $R_N \ll 1$) if $N \gg \frac{\log(1-t)}{\log t}$ (Fig. A1).

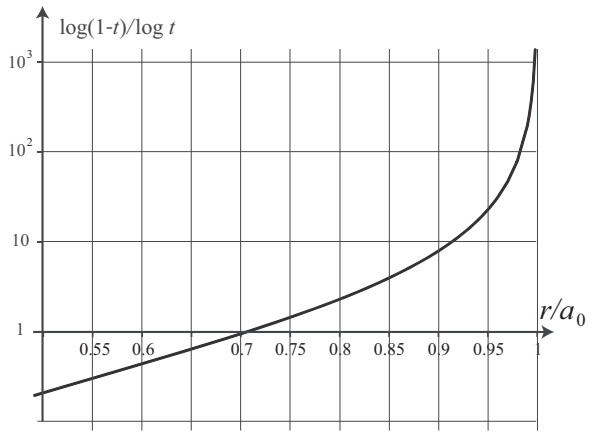

Figure A1. For each r/a_0, if the number N of terms is located above the curve $\log(1-t)\log t$ as function of r/a_0, a good approximation of the series in eq. (49) is obtained.

Thus, only few terms are sufficient to provide a proper evaluation of the series (eq. 49) as far as $r/a_0 < 0.7$ but the number N increases rapidly to 10 if $r/a_0 = 0.9$, to 200 if $r/a_0 = 0.99$ and becomes infinite when $r/a_0 \to 1$ (Fig. A1). If $r > a_0$ we may prove in a similar way that the series (eq. 39) is absolutely convergent and continuous. Fig. 4(a) shows u_r versus r for a few values of θ, and Fig. 5(a) shows u_r versus θ for a few values of r.

When $r \simeq a_0$ (near the boundary between the inner and outer domain) the series in eq. (49) diverges logarithmically to $+\infty$ when $\theta \to \frac{\pi}{2}$ (Fig. 4a) and $t \to 1$ since $P_{2m}(0) = c_{2m}$ and the mth term in the series, according to eq. (30), is asymptotically greater than $\frac{1}{\pi\sqrt{t}} \frac{t^m}{m}$ (remind that $\log(1-t) = -\sum_{m=1}^{\infty} \frac{t^m}{m}$ if $t < 1$). The singularity may be eliminated considering that the equivalent body force system generating $\frac{\partial G_{ij}}{\partial x_j}$ in eq. (10) is actually distributed over the volume $V_s = \pi a_0^2 b$ with small but finite thickness b instead of the flat disc surface πa_0^2; this means that the solution (eq. 49) is valid only if $a_0 - r \gg b$. Similar considerations hold for the series (eq. 39) describing u_r in the external domain.When $r \to a_0$ along directions $\theta \neq \frac{\pi}{2}$, convergence may be achieved thanks to the sign oscillations of the product $c_{2m} P_{2m}(x)$, but the rate is extremely slow. In these cases, the value of u_r in $r = a_0, \ \theta \neq \frac{\pi}{2}$ may be obtained through analytic continuation starting from values computed at $r/a_0 < 1$ or, more efficiently, through interpolation between points $r_1/a_0 < 1$ and $r_2/a_0 > 1$, where convergence is achieved at reasonably fast rates (Fig. 4a inset).

A2 Polar component of displacement (eq. 50)

Let us consider the polar component u_θ and the series in eq. (50); since $\left|\frac{\mathrm{d}P_{2m}}{\mathrm{d}\theta}\right| \leq m(2m+1)$ (see e.g. Abramowitz & Stegun 1965), the rest of the series of absolute values is

$$R_N < t \sum_{N+1}^{\infty} m t^m,$$

where $t = \left(\frac{r}{a_0}\right)^2$. Using D'Alambert criterion, $\sum m t^m$ is absolutely convergent since the ratio of consecutive terms $\frac{(m+1)t^{m+1}}{mt^m} = \frac{m+1}{m}t$ tends asymptotically to a limit $t < 1$. The number N of terms required to make $R_N \ll 1$ may be evaluated from

$$R_N < \sum_{N+1}^{\infty} q^m < \frac{q^{N+1}}{1-q},$$

where q is computed from the requirement that $mt^m < q < 1, \forall m > N$. The sequence mt^m decreases while m increases if $m > \frac{t}{1-t}$. Thus, once $N > \frac{t}{1-t}$ we may pose $q = (N+1)t^{N+1}$ and $R_N \ll 1$ if $N \gg \frac{\log(1-q)}{\log q}$. When $r = a_0$ and $\theta \neq \frac{\pi}{2}$ the series describing u_θ are not convergent (a necessary requirement for convergence of a series is that its mth term vanishes when $m \to \infty$), but analytic continuation may be used to compute their values if $\theta \neq \frac{\pi}{2}$. If $r = a_0$ and $\theta = \frac{\pi}{2}$ the mentioned series vanish because all $\frac{\mathrm{d}P_{2m}}{\mathrm{d}\theta}$ vanish.

A3 Strain components (eqs 53–64)

Absolute convergence of the series describing the strain components (eqs 53–64) when $r \neq a_0$ is proved in a similar way and the number of terms required to provide a fair approximation may be computed according to the same scheme used for u_θ. When $r = a_0$ all the mentioned series are not convergent but analytic continuation may be used to compute their values if $\theta \neq \frac{\pi}{2}$. If $r = a_0$ and $\theta = \frac{\pi}{2}$ all the mentioned series are divergent to $\pm\infty$ apart from $\epsilon_{r\theta}$ (eqs 63 and 64) which vanish if $\theta = \frac{\pi}{2}, \forall r$ but is singular in $r = a_0$ because no definite limit exists in a neighbourhood of $r = a_0, \theta = \frac{\pi}{2}$ (Fig. 7d dashed line).